

**PHYSICAL CONDITIONS IN THE SEYFERT GALAXY NGC 2992**MARK G. ALLEN<sup>1</sup>, MICHAEL A. DOPITA<sup>1</sup>, ZLATAN I. TSVETANOV<sup>2</sup> AND RALPH S. SUTHERLAND<sup>1</sup>**ABSTRACT**

This paper presents long slit spectral maps of the bi-cone shaped extended narrow line region (ENLR) in the Seyfert galaxy NGC 2992. We investigate the physical properties of the ENLR via emission line diagnostics, and compare the observations to shock and photoionization models for the excitation mechanism of the gas. The line ratios vary as a function of position in the ENLR, and the loci of the observed points on line ratio diagrams are shown to be most consistent with shock+precursor model grids. We consider the energetics of a nuclear ionizing source for the ENLR, and perform the  $q$ -test in which the rate of ionizing photons from the nucleus is inferred from measurements of the density and ionization parameter. The  $q$ -test is shown to be invalid in the case of NGC 2992 because of the limitations of the [S II]  $\lambda 6717/\lambda 6731$  density diagnostic. The excitation of the gas is shown to be broadly consistent with the kinematics, with higher [N II]  $\lambda 6583/H\alpha$  present in the more dynamically active region. We also show that the pressure associated with the X-ray emitting plasma may provide a large fraction of the pressure required to power the ENLR via shocks.

*Subject headings:* galaxies: active — galaxies: individual (NGC 2992) — galaxies: Seyfert

**1. INTRODUCTION**

The narrow line regions (NLR) of active galaxies are the largest structures which directly derive their energy input from the active galactic nucleus (AGN). In many nearby Seyfert galaxies the NLR are spatially resolved, and often extend over distances of several kpc, so that the energy input processes may be studied in detail. Such spatially-resolved NLR are often referred to as

---

<sup>1</sup>Mount Stromlo and Siding Spring Observatories, The Australian National University, Private Bag Weston Creek P.O., ACT 2611, Australia; mga, mad, ralph@mso.anu.edu.au

<sup>2</sup>Department of Physics and Astronomy, Johns Hopkins University, Baltimore MD 21218, USA; zlatan@pha.jhu.edu

extended narrow line regions (ENLR) (Unger et al. 1987). In both Seyfert 1 and Seyfert 2 galaxies the ENLR appears as a filamentary system of high excitation gas and in Seyfert 2 galaxies this gas is often confined to a bi-cone structure centred on the nucleus, the so called “ionization cones”. In other cases, the morphology is more complex, and bent jet-like structures are sometimes observed.

According to the model developed some twenty years ago (Koski 1978; Ferland & Netzer 1983; Stasinska 1984), and which remains the dominant paradigm (Robinson et al. 1987, Viegas & de Gouveia Dal Pino 1992), the NLR are excited by photoionization by a powerful (approximately power-law) non-thermal UV continuum produced by the AGN. This scenario appeals to the unified schemes for AGN in which the nucleus and the broad-line region are surrounded by an optically thick torus (Antonucci & Miller 1985). In this picture the differences between Seyfert types 1 and 2 are ascribed to an orientation effect in which type 1 Seyferts are oriented so that the line of sight falls within the opening angle of the cones, while in type 2 Seyferts the line of sight to the nuclear region is obscured by the torus. This scenario explains the conical ENLR observed in some type 2 Seyferts as due to shadowing of the ionizing radiation from the nucleus by the absorbing torus.

Shocks may also be important for the morphology, kinematics and excitation of the NLR in Seyfert galaxies. In some Seyferts the morphology of the emission line gas is directly related to that of the radio emission, providing evidence for dynamical interaction between the radio plasma and the ambient interstellar medium of the host galaxy. For example, high resolution narrow band imaging with HST has revealed bow-shock shaped emission line regions around radio lobes, and jet-like emission line regions in sources with jet-like radio structures (Axon et al. 1998, Pogge 1996, and references therein).

Shocks probably dominate the physics of the large scale outflows observed in Seyfert galaxies. In a series of papers, (Colbert et al. 1996a, Colbert et al. 1996b, Colbert et al. 1998) Colbert and collaborators show that optical emission suggestive of large scale outflows is present in  $\gtrsim \frac{1}{4}$  of their sample of 22 edge-on Seyfert galaxies,  $\gtrsim \frac{1}{2}$  of the sample have kiloparsec scale radio structures, and 3 of their sample, including NGC 2992, have similarly extended soft X-ray emission. Colbert et al. (1998) favour an interpretation in which these large scale outflows originate as AGN driven non-thermal jets that entrain the surrounding thermal material, and heat it by shocks over kpc spatial scales. An alternative possibility is that the X-ray gas results from starburst driven winds from the circumnuclear region.

Seyfert galaxies are radio quiet, and simple equipartition arguments have long suggested that the pressure in the relativistic plasma responsible for the radio wavelength synchrotron emission is inadequate to drive high velocity shocks into the interstellar medium (Wilson, Ward, & Haniff 1988). However, this picture may be wrong if mass entrainment into the jet occurs close enough to the source. Recently Bicknell et al. (1998) has shown that although the radio jets of Seyferts start off mildly relativistic, over most of their length the internal energies of Seyfert jets must be dominated by thermal plasma. The combined pressure of the thermal and relativistic gas is then sufficient for the jets to power the optical emission of the NLR. This idea finds observational

support from the work of Colbert et al. (1998) which suggests that the large scale outflows in Seyfert galaxies are predominantly winds of thermal X-ray emitting gas. This thermal phase will dominate the pressure, consistent with the requirements of the theory described in Bicknell et al. (1998).

Models of shocks for Seyfert galaxies have considered various scenarios for the excitation of the gas. Bow-shock models developed by Taylor, Dyson & Axon (1992) (which can account for the wide range of line profile shapes observed in the NLR) consider the excitation mechanism to be photoionization, whereby the shocks simply serve to compress the gas which is then illuminated by UV continuum from the nucleus. More recent models show that shocks themselves can provide an alternative mechanism for the ionization of the NLR based on the input of mechanical energy. These shock models advanced by Sutherland, Bicknell & Dopita (1993) and developed in detail by Dopita & Sutherland (1996) show that high velocity shocks generate strong UV radiation in the high temperature cooling zone behind the shock front, the hardness of which depends on the shock velocity. This photon field is then available to produce a highly ionized precursor H II region, which emits a spectrum like that observed in the NLR. Dopita & Sutherland (1995) find that their shock+precursor models can account for the observed optical emission line ratios of a sample of Seyfert galaxies. This raised the possibility that such models may be generally applicable to narrow emission line regions.

In order to find observational support in favour of either the shock or the photoionization model of the NLR, we have undertaken a detailed spectroscopic and dynamical study of the ENLR of a number of nearby Seyferts. Amongst these, the subject of this paper, NGC 2992 provides a particularly good test case to compare the predictions of the models with observations. NGC 2992 is a gas-rich (Hutchmeier 1982; Sanders and Mirabel 1985) Sa type galaxy classified as having a Seyfert 1.9 active nucleus. It is inclined at  $\sim 70^\circ$  to our line of sight and is crossed by a disturbed dust lane. It is interacting with NGC 2993 which is connected to the southern part of NGC 2992 by a tidal tail with a projected length of  $2.9'$ . The nuclear redshift is  $z=0.0077\pm 0.0002$  which gives angular scale  $150 \text{ pc arcsec}^{-1}$  assuming  $H_0=75 \text{ km s}^{-1} \text{ Mpc}^{-1}$ .

It provides an interesting test case because it displays a striking and unusually extensive bi-conical ENLR which emerges almost perpendicularly from the plane of the galaxy. Narrow band images show the spatial extent of bright bi-cones is  $\sim 4 \text{ kpc}$ , with the SE cone brighter than the NW cone. Fainter emission is extended up to  $8 \text{ kpc}$ . Figures 1a and 1b show narrow band filter images obtained at the ESO New Technology Telescope (NTT). These are respectively  $[\text{O III}] \lambda 5007$ , and  $\text{H}\alpha + [\text{N II}]$  and are presented on a logarithmic stretch so as to bring out the fainter regions. Figure 1c shows a blue continuum image of NGC 2992.

The radio structure of NGC 2992 is described in detail in a paper by Wehrle & Morris (1988) which includes a synopsis of previous radio observations. In summary NGC 2992 has  $20 \text{ cm}$  radio emission which extends approximately  $25''$  along  $\text{PA} \sim 160^\circ$ , and has a one sided extension along  $\text{PA} \sim 130^\circ$ . At a wavelength of  $6 \text{ cm}$  there is visible a smaller scale figure-8-shaped structure, with

its long axis extending approximately  $8''$  along  $PA \sim -26^\circ$ , and centred on the nucleus. The figure-8 may represent edge brightened bubbles of relativistic plasma or else magnetically-compressed arches, either of which are indicative of an expanding region of over-pressured relativistic plasma. However, comparison of the radio images with optical narrow band images shows no obvious correlation between the structures - see Figures 1d, 1e and 1f where these radio maps are overlaid on our [O III]  $\lambda 5007$ , and continuum images.

NGC 2992 was included in Durret and Bergeron's investigation of the physical properties of the ionized gas in emission line galaxies (Durret and Bergeron 1988, Durret 1990). In the earlier paper they present long slit observations of NGC 2992. The second paper describes the physical properties of the ionized gas and other general characteristics derived from their spectra. Here we briefly summarise their results.

First, in the nuclear spectrum a broad component of  $H\alpha$  is detectable, but there is no corresponding broad  $H\beta$  component. NGC 2992 is therefore classified as an intermediate type Seyfert (1.9). This classification is confirmed from the shape of the far-IR to far-UV continuum (Boisson and Durret 1986). Second, Durret and Bergeron (1988) found the extranuclear spectra along  $PA = 197^\circ$  have similar line ratios to the nuclear region, and are characteristic of those found in Seyfert 2 galaxies. This excludes the possibility that the ENLR is excited by OB stars. The excitation of the gas appears to decrease from the nucleus to the outer regions. The reddening of the inner regions is high, ranging up to  $A_v \sim 3$ , and a similar reddening was estimated by Malkan (1983) from the [S II]  $\lambda\lambda(4069+4076)/(6717+6731)$  ratio. Third, using the  $H\alpha/H\beta$  to correct line ratios for reddening Durret and Bergeron (1988) found a temperature of  $T_e = 19900\text{K}$  from the [O III] lines in the nuclear regions.

The velocity field of NGC 2992 is complex. A kinematical study by Colina et al. (1987) revealed blue asymmetries in the [O III] lines at the center of the galaxy, and showed that the nuclear region is dynamically decoupled from the off-nuclear regions. Colina et al. (1987) find some indication of radial outflow within a plane highly inclined to the galaxy plane, and that the kinematics of the SE region may be accounted for by tidal interaction with NGC 2993. Recently Márquez et al. (1998) have reported a kinematical study of NGC 2992 with the  $H\alpha$  and [O III] lines measured along nine position angles. They note that outflow of the gas within a conical envelope or on the surface of a hollow cone as one possible picture to account for the double peaked profiles and asymmetries detected in several regions. However they use a simple kinematical model of circular rotation with a constant radial outflow, where the out-flowing velocities are considered as radial motions in a plane very close to that of the gas disk. While this model provides a good approximation to the observed kinematics we caution that such a model is not unique, and prefer to interpret the kinematics as a general outflow or wind, not necessarily constrained to a particular plane. This was reported briefly by us in Tsvetanov, Dopita & Allen (1995) and details will appear in a future paper. In summary, our higher spectral resolution study of the NGC 2992 NLR shows double component line profiles at most positions. One of the kinematical components follows a galactic rotation curve, while the other component is identified as a wind which is expanding out

of the plane of the galaxy with velocities up to  $200 \text{ km s}^{-1}$ .

These kinematical studies generally assume the disk of NGC 2992 to be oriented with NW edge closest, in concordance with trailing spiral arms. In this orientation, with the axis of the bi-cone perpendicular to the disk, the SE cone is the closer and is directed towards us, consistent with the outflow interpretation. If on the other hand the spiral arms lead, then the SE edge of the galaxy and the NW cone would be closer. In this orientation the kinematics would indicate inflow instead of outflow. Other possibilities also exist if the bi-cone axis is highly inclined with respect to the galaxy disk.

The X-ray spectral properties of NGC 2992 are described by Weaver et al. (1996) (and references therein) to have a significant absorbing column and a prominent Fe  $K\alpha$  fluorescence emission line. The X-ray flux varies by a factor of 2–3 on timescales of days to months. There is an excess of soft X-ray (0.1–2.0 keV) flux above that expected from the extrapolation of the 2–10 keV power law ( $\Gamma=1.7$ ), and there is also some evidence for extended soft X-ray emission on a scale of  $\sim 2$  kpc. X-ray images of NGC 2992 taken with the *ROSAT* Position Sensitive Proportional Counter (PSPC), and High-Resolution Imager (HRI) are presented by Colbert et al. (1998). Soft X-ray (0.2 – 2.4 keV) emission extends out to  $\sim 1'$  along  $PA \sim 100^\circ$ , and is roughly co-spatial with the 20 cm radio emission.

Recently Glass (1997) have reported that the near infrared light-curve of NGC 2992 (monitored  $\sim 3$  times a year over the past 15 years, with an  $9''$  aperture) shows an outburst in 1988. The amplitude of the event was greatest in the L( $3.5 \mu\text{m}$ ) band, which increased 102 mJy above the base level in less than 254 days, then decayed exponentially with an e-folding time of  $\sim 900$  days. Glass (1997) compare the total energy output of the event ( $6 \times 10^{43}$  J) to the explosion energies of types I and II supernovae. They find that while a conventional un-obscured supernova does not provide a direct fit, the outburst may be explicable in terms of a model similar to that of Terlevich et al. (1992), which seeks to explain the characteristics of Seyfert nuclei in terms of multiple supernova explosions in dense H II regions.

This paper presents the results of mapping the ENLR of NGC 2992 with long slit spectroscopy in order to investigate the detailed spatial dependence of line ratios and the physical properties with the objective of understanding the mode of excitation of the ENLR. The observations and data reductions are described in section 2, including the line flux measurements and representative spectra. Three distinct spectral regions of the ENLR are identified in section 3 in which we show the spatial variation of the line ratios. In section 4 we derive the physical properties of the emission line gas. The observations are compared to shock and photoionization model predictions with line ratio diagnostic diagrams in section 5. We discuss the  $q$ -test for photoionization from a central source in section 6. In section 7 we compare the excitation of the gas with the kinematics, and consider the possibility of a thermal pressure energy source for the excitation of the ENLR.

## 2. OBSERVATIONS AND DATA REDUCTION

NGC 2992 was observed with the Double Beam Spectrograph (DBS) on the ANU 2.3m telescope at Siding Spring, Australia on March 5th and 9th 1994. Loral CCD detectors were used on both the red and blue arms of the spectrograph. The 158 line  $\text{mm}^{-1}$  grating was used in the red arm giving a dispersion of  $4.1 \text{ \AA pixel}^{-1}$ , a spectral resolution of  $11.9 \text{ \AA}$  and covering a wavelength range 5840–9725  $\text{\AA}$ . The 300 line  $\text{mm}^{-1}$  grating was used in the blue arm, providing a dispersion of  $2.2 \text{ \AA pixel}^{-1}$ , and yielding a  $4.9 \text{ \AA}$  spectral resolution over the wavelength range 3440–5570  $\text{\AA}$ . The slit width was fixed at  $2''$  for all observations of NGC 2992, but was increased to  $5''$  for observations of standard stars so as to ensure that slit losses were negligible. The spatial scale along the slit was the same in both red and blue arms;  $0''.89 \text{ pixel}^{-1}$ .

Spectra were obtained for a total of nine slit positions all orientated at PA  $30^\circ$ . These were placed  $\sim 2''$  apart so as to efficiently cover the ENLR and provide a set of spatially independent spectra. A total of three 1000 s exposures were taken at each slit position. The FWHM of the standard star profiles along the wide slit provides an estimate of the seeing plus the guiding errors. At the beginning of the first night the median seeing was  $\sim 2''$  but improved to  $\sim 1''.8$  by the end of the night. The seeing in the middle of the second night was  $\sim 2''.3$ .

Data reduction was performed using the standard IRAF routines. Pixel to pixel variations in the CCD response were removed by appropriately normalised spectral flat fields derived from Quartz-Iodine lamp spectra, while a correction for the slit function was made by a low order fit to the illumination of the slit by the twilight sky. The DBS has very low vignetting, so this correction is not very important. The wavelength scale was established by fitting 5th order Chebychev polynomials to lines identified in Helium-Argon comparison lamp spectra obtained throughout the observations on both nights.

Long-slit observations are usually affected by misalignments and optical distortions which cause the dispersion direction not to be exactly aligned along the lines of the CCD. Spectra of standard stars through a narrow slit revealed this effect to be of order 2.5 pixels over the 1000-pixel length of the CCD, and the arc lines are tilted by approximately 2 pixels. The distortion in each object and standard star frame was found by tracing the continuum along the dispersion direction. The distortion in the slit direction was similarly found by tracing the lines in the arc frames. Two dimensional fits to the wavelength and geometrical correction as a function of position was done with the IRAF task *fitcoords*. The two transformations were inverted to map the wavelength as a linear function along lines of the frame, and the position along the slit as a linear function along the columns. The subtraction of the background sky contribution could then be performed, having first normalised the spectra by fitting a 2nd order polynomial to the background in each column.

All frames were divided by a smoothed spectrum of a featureless DC white dwarf star in order to remove the effects of the dichroic transmission variability, which because of interference effects is a complex oscillatory function of wavelength. The sensitivity function derived from the measured standard stars can then be fit by a low order polynomial. The spectrophotometric standards L745-

46A and W485A were used to calibrate the absolute fluxes of the spectra on the first night, while only L754-46A was observed on the second night. The nights appeared to be photometric, with atmospheric transmission varying less than 10%. No attempt was made to remove the atmospheric molecular absorption bands.

An error frame was calculated for each 2-dimensional spectrum by taking the square root of the counts after the instrumental corrections and propagating the error through the reductions.

Since the observations were made without the aid of an auto-guider, and the slit positions were set up by offsetting from the nuclear peak of light as it appeared in the TV display, the slit positions were not very accurately controlled. More accurate slit positions were found by matching the intensity profile of the brightest line in the spectrum [O III]  $\lambda 5007$  to the intensity profile generated from an narrow band image of the galaxy in this same emission line. This technique involves firstly rotating and binning the image to the same pixel scale and spatial orientation as the 2-d spectra ( $0''.89 \text{ pixel}^{-1}$ , PA  $30^\circ$ ). Simulated intensity profiles for slits positioned at  $0''.3$  steps across the ENLR were then generated from the image, and were compared to the observed slit profiles. The best match in each case was found by cross-correlating the observed intensity profile with the set of simulated slit profiles. The IRAF task *fxcor* was used in its pixel correlation mode for this purpose. The correlation function calculated for each simulated slit with the observed profile is a measure of how well the simulated profile matches the observed profile, and gives the relative shift in pixels between the two profiles. The height of the correlation functions provide three or four best match candidates, which are then inspected manually and a best match chosen. For all but slits -5 and 3 the best match was obvious upon inspection so in general we regard the slit positions as known to within  $0''.3$ . The derived slit positions are shown overplotted on the [O III]  $\lambda 5007$  image contours in Figure 2. In the remainder of the paper we refer all spatial positions in the ENLR of NGC 2992 to the coordinate system shown in this figure.

The relative and absolute flux calibrations of all slits was assessed by extracting the flux of [O III]  $\lambda 5007$  from the calibrated narrow band image at the  $x, y$  coordinates of the spectra and comparing with the line flux measured from the spectra. The spectra and image fluxes match within 20% at most  $x, y$  positions.

One dimensional spectra were extracted from the long slit frames by summing every three pixels along the slit. The  $y$  coordinate of the extraction is known from the  $y$  position of the best match simulated slit, and the  $x$  coordinates are determined from the relative shift given by the cross-correlation. This results in a grid of spectra covering the ENLR of NGC 2992 with a spacing of approximately  $2''$  in the  $y$  direction, and closer spacing in the  $x$  direction. To improve the signal-to-noise ratio in the faint, outer regions of the ENLR we have co-added up to 8 spectra into a more coarse grid.

Average spectra of the NW cone, SE cone and inter-cone regions of the ENLR are shown in Figures 3a, 3b and 3c. A sky feature is seen at  $6860 \text{ \AA}$  and the red end of the spectra are not shown as that region is contaminated with sky features.

## 2.1. Emission line measurements

The fluxes, wavelengths and widths of the bright emission lines were measured in each grid point spectrum by fitting Gaussians to the line profiles with a linear fit to the continuum in the wavelength region of the line. We find that approximating the continuum as a linear function does not significantly affect the measurement of the bright lines. The bright emission line measurements were done with the IRAF STSDAS task *specfit*. For the [S II], [N II] and [O III] doublets the FWHM and wavelength ratio of the lines were fixed in the fitting procedure.  $1\sigma$  uncertainties in the flux, wavelength and FWHM measurements were calculated from the error spectrum derived from the error frames described above.

## 2.2. Subtraction of the stellar population and faint line measurements

At all locations in the ENLR the emission line spectrum is superimposed on an underlying galaxy stellar spectrum. Figure 3b shows that the galaxy contribution is much stronger on the SE side of the galaxy. The main stellar features are readily identified as the Ca H and K bands, the G band of C-H at 4290–4313 Å, H $\beta$  absorption, Mg b at around 5170 Å and Na I 5890–5896 Å. We find that these stellar features and the general shape of the underlying galaxy spectrum can be matched by the spectrum of the E4 peculiar galaxy NGC 1316 (Pickles 1985) with some correction for reddening.

Subtraction of the stellar population is very important for the detection and measurement of faint emission lines. Storchi-Bergmann et al. (1996) emphasize the importance of subtracting stellar features to obtain accurate measurements of the H $\gamma$ , [O III]  $\lambda$ 4363, and He II  $\lambda$ 4686 lines in ENLR spectra. Using Storchi-Bergmann et al. (1996) as a guide for matching the stellar features we have fitted the observed spectra of the NW and SE cones, using the NGC 1316 galaxy template to account for the underlying galaxy continuum. The fit was done over the wavelength range 4200–5300 Å, with the IRAF *specfit* package. In the fitting procedure we constrain the redshift of the template to a range close to that determined for the emission lines in the spectrum. A reddening correction is applied in the fitting procedure using the Cardelli, Clayton, & Mathis (1989) reddening curve and allowing E(B-V) to be a free parameter. The emission lines H $\gamma$ , [O III]  $\lambda$ 4363, He II  $\lambda$ 4686, H $\beta$ , the [O III]  $\lambda\lambda$ 4959,5007 doublet and [N I]  $\lambda$ 5200 were included in the fit as Gaussian components. The widths of the H $\gamma$  and H $\beta$  lines were linked to have the same value in the fit, as were the widths of the [O III]  $\lambda\lambda$ 4959,5007 doublet lines. [O III]  $\lambda$ 4363 was not linked to the other [O III] lines because the asymmetry observed in the brighter [O III] lines is not seen in the the fainter [O III]  $\lambda$ 4363 line. An error spectrum derived from the original photon statistics of the CCD observations was used in the fitting procedure and allows the calculation of uncertainties in all the fit parameters. The  $1\sigma$  uncertainties in the NW and SE cone spectra are approximately 0.15 and  $0.4 \times 10^{-16}$  ergs s $^{-1}$  cm $^{-2}$  Å $^{-1}$  respectively over the wavelength range of the fit.

The NW cone and SE cone spectra are both well fit by this procedure, with the template



galaxy component matching the wavelengths and depths of the stellar absorption features. The underlying galaxy spectra in the NW cone required an  $E(B-V)$  of 0.16 and the SE cone required an  $E(B-V)$  of 0.17. Figures 4a and 4b show the result of the fits for the NW and SE cones respectively where we show the galaxy template component overplotted on the observed spectra. For each case we have also subtracted the fitted galaxy template spectrum to reveal the spectrum of the emission line gas. A small amount of residual structure is seen the spectrum after template subtraction, however this structure is within the  $1\sigma$  noise level. The template subtracted spectrum of the NW cone clearly shows the  $H\gamma$ ,  $[O III] \lambda 4363$  and  $He II \lambda 4686$  lines. In the SE cone  $H\gamma$  and  $He II \lambda 4686$  are clearly seen, but  $[O III] \lambda 4363$  is only just above the noise level resulting in a relatively uncertain measurement of the  $[O III] \lambda 4363$  flux for the SE cone.

### 2.3. Reddening correction

NGC 2992 has a prominent dust lane and the observed spectra show that the reddening varies as a function of position in the ENLR, and that the reddening derived from the emission lines is higher than for the underlying galaxy spectrum. The most severely reddened spectra occur in the regions associated with the dust lane, with the  $H\alpha/H\beta$  ratio observed as high as 10. For each grid point spectrum where both  $H\alpha$  and  $H\beta$  are detected we derive a value of the reddening from the  $H\alpha/H\beta$  ratio, using the reddening curve of Cardelli, Clayton, & Mathis (1989) and assuming an intrinsic  $H\alpha/H\beta$  ratio of 3.1. The reddening within the dust lane thus corresponds to  $A_V=3.6$  and decreases outwards along the  $y$  direction away from the dust lane. The average reddening values in the NW and SE cones are  $A_V=0.86$  and 1.8 respectively. With the orientation of NGC 2992 described in section 1, we might expect the NW cone, seen through the disk of the galaxy to have the greater reddening. The disturbed nature of the dust lane may account for this discrepancy.

The emission line measurements for the average spectra of the NW and SE cone, and inter-cone regions are given in Table 1 along with their reddening corrected values. In each case the line fluxes are given relative to  $H\beta=100$ .

## 3. RESULTS

The spectra of the ENLR of NGC 2992 are typical of Seyfert 2 type galaxies with strong lines of  $[O III] \lambda 5007$ ,  $[O II] \lambda 3727$ ,  $H\alpha$  and also the low ionization lines  $[S II] \lambda\lambda 6717, 6731$ ,  $[N II] \lambda 6583$  and  $[O I] \lambda 6300$ . Highly ionized Iron lines (Fe VII, Fe IX, Fe X) sometimes seen in Seyfert galaxies are not detected in our spectra.  $[Ne V] \lambda 3426$  is detected at the far blue end of the wavelength range, and the  $[S III] \lambda\lambda 9069, 9532$  lines are detected but are strongly affected by night sky features. We also detect a blue asymmetry in the line profiles of the  $[O III] \lambda\lambda 4959, 5007$  lines in the SE cone. The fainter lines of  $[O III] \lambda 4363$ ,  $H\gamma$  and  $He II \lambda 4686$  are also detected in co-added spectra of the NW and SE cones.

### 3.1. Spatial variation of the spectra

A striking feature of this set of spectra is the strong variation of the line ratios as a function of position in the ENLR. Figure 5a shows how the  $[\text{O III}] \lambda 5007/\text{H}\beta$  and  $[\text{N II}] \lambda 6583/\text{H}\alpha$  line ratios separate the spectra of the ENLR into three groups that correspond to different regions within the ENLR. The open circles indicate spectra extracted from the NW cone of the ENLR, the filled squares are for points within the SE cone, and the open triangles correspond to spectra extracted from regions between the two cones, and from the outer edges of the two cones.

This effect is shown even more clearly in Figure 5b where we have used the ratio of  $[\text{O III}] \lambda 5007$  to  $\text{H}\alpha$  instead of  $\text{H}\beta$ . Using the brighter  $\text{H}\alpha$  line allows us to include spectra down to a fainter brightness limit, thus covering more of the ENLR, especially those fainter regions between the cones. The disadvantage of using the  $[\text{O III}] \lambda 5007/\text{H}\alpha$  ratio is that the reddening correction is greater than the correction to  $[\text{O III}] \lambda 5007/\text{H}\beta$ . This larger reddening correction with its greater uncertainty causes more scatter of the points in Figure 5b. For the faintest regions where  $\text{H}\beta$  is not detected, we have applied a value for the reddening which has been extrapolated from adjacent points at which  $\text{H}\beta$  is measured. This procedure is most uncertain for the spectra extracted from points between the cones and within the dust lane of the galaxy. For these points we apply the average reddening of the dust lane points which is equivalent to assuming an  $\text{H}\alpha/\text{H}\beta$  ratio of 6 before reddening correction. Despite these uncertainties in the reddening correction for the  $[\text{O III}] \lambda 5007/\text{H}\alpha$  ratio, the inferred spatial variation of the line ratios remains similar to those found in Figure 5a.

Figure 6 shows the spatial locations of the spectra used in Figures 5a and 5b. We shall maintain the distinction between these three spatial regions by using the same plotting point styles throughout the rest of this paper.

### 3.2. $[\text{N II}]/\text{H}\alpha$ variation

Figures 5a and 5b show that the the NW and SE cones have significantly different  $[\text{N II}] \lambda 6583/\text{H}\alpha$  ratios. The  $[\text{N II}] \lambda 6583/\text{H}\alpha$  ratio of the average spectrum of the NW cone is 0.46 compared to 0.76 for the SE cone.

Since the SE cone has a stronger underlying galaxy continuum we have investigated the possibility that the variation in  $[\text{N II}] \lambda 6583/\text{H}\alpha$  between the two cones is due to a greater amount of  $\text{H}\alpha$  absorption in the SE cone. To test this possibility we use the fit to the blue region of the underlying stellar distribution that was discussed in the previous section, and apply it to the spectral range around the  $\text{H}\alpha$  and  $[\text{N II}]$  lines. In the spectral region around  $\text{H}\alpha$  it is more difficult to make an independent fit for the underlying galaxy continuum. We therefore fit the galaxy template in the 6450–6700 Å spectral range using the same multiplicative scale and reddening parameters derived for the blue region. The  $\text{H}\alpha$  line and each of the  $[\text{N II}] \lambda\lambda 6548, 6583$  emission lines are fitted with single component Gaussian profiles with the fit constrained so that the  $[\text{N II}]$  doublet

line wavelengths were at the known ratio. For the fit the flux ratio  $[\text{N II}] \lambda 6583/\lambda 6548$  was fixed at 3.0, and both  $[\text{N II}]$  components were constrained to have the same line widths.

The results of the fits to the NW cone and SE cone and dust-lane region spectra over the 6450–6700 Å range are shown in Figure 7. In each panel we show the total fit overlaid on the data and also the result of subtracting the template from the data. The lighter weight curves in Figure 7 show the fitted galaxy template and the individual Gaussian component fits to the  $\text{H}\alpha$  and  $[\text{N II}]$  emission lines.

We obtain an excellent fit to the spectrum in the NW cone. Since the stellar contribution is faint in this cone there is only a small amount of  $\text{H}\alpha$  absorption which is barely discernable in the plot, and is insignificant relative to the emission line fluxes. The fit to the SE cone (middle panel of Figure 7) demonstrates that stellar  $\text{H}\alpha$  absorption is more important on the SE side of the ENLR. This has the effect of increasing the  $\text{H}\alpha$  flux measurement by  $< 5\%$  and decreases the  $[\text{N II}] \lambda 6583/\text{H}\alpha$  ratio by  $< 7\%$  compared to the values obtained by using a linear continuum level in the measurement of these lines. This is not large enough to make a significant difference to the  $[\text{N II}] \lambda 6583/\text{H}\alpha$  ratio. We have thus established that the variation of the ratio between the NW and SE cones cannot be attributed to  $\text{H}\alpha$  absorption, and must therefore be due to real physical differences between the excitation conditions in the cones.

The slight excess shown by the fit at the wavelength of the  $[\text{N II}] \lambda 6548$  line is most likely due to a blue asymmetry in the  $\text{H}\alpha$  line similar to the asymmetry in the  $[\text{O III}] \lambda 5007$  line seen at the same location. While it is possible to add another component of  $\text{H}\alpha$  to obtain a better fit to the spectrum, we would also need to include similarly blue shifted  $[\text{N II}]$  components, and this data simply do not have the resolution or signal to noise required to properly constrain the relative fluxes or line widths of such additional components.

The lower panel of Figure 7 shows the fit to the brightest point in the dust-lane region of the ENLR. Here  $\text{H}\alpha$  and the  $[\text{N II}]$  lines are well fitted by single component Gaussians, and yield a  $[\text{N II}] \lambda 6583/\text{H}\alpha$  ratio of  $0.59 \pm 0.01$  which is intermediate to the values measured in the NW and SE cones.

## 4. Physical properties of the emission line gas

### 4.1. Temperature

The  $[\text{O III}] \lambda 4363/[\text{O III}] \lambda 5007$  line ratio is the well known temperature diagnostic often referred to as  $R_{\text{OIII}}$ . We estimate the temperature from  $R_{\text{OIII}}$  using the IRAF STSDAS *nebular* package which draws on the atomic data of Mendoza (1983) for the  $\text{O}^{+2}$  ion. An assumed density of  $100 \text{ cm}^{-3}$  was used in the temperature calculation, and we note that the calculation is relatively insensitive to density. The average spectrum of the NW cone has  $R_{\text{OIII}}=0.019 \pm 0.004$  corresponding to  $T_e=14780_{-980}^{+1550}$ . The average spectrum of the SE cone has  $R_{\text{OIII}}=0.025 \pm 0.009$  corresponding

to  $T_e = 16990^{+5600}_{-2300}$ , the greater uncertainties in the SE cone are due to the large uncertainty in the [O III]  $\lambda 4363$  measurement. These temperatures are lower than the value of 19900 K obtained by Durret and Bergeron (1988) for the nuclear region. It is well known that temperature fluctuations in the ionized region tend to drive the value of  $R_{OIII}$  up, so the measured temperatures are probably somewhat higher than the mean temperature characterising the  $O^{+2}$  zone.

## 4.2. Density

The ratio of [S II]  $\lambda 6717$ /[S II]  $\lambda 6731$  is a density diagnostic sensitive in the range  $100\text{--}10000\text{ cm}^{-3}$ . Density estimates from the [S II] ratios were calculated with the IRAF STSDAS *nebular* package which draws on the atomic data of Cai & Pradhan (1993) for the  $S^{+1}$  ion. Figure 8 shows these densities plotted against the projected radius of the spatial locations within the ENLR. The average error bar on the density measurements is approximately  $80\text{ cm}^{-3}$ . We find that the [S II] ratios are close to the lower limit of the diagnostic range, and that some points have [S II] ratios which can only be used as an upper limit for the density. The central regions have the higher density values. Although Figure 8 shows a general trend of decreasing density with distance from the nucleus, the densities in the cones (when these can be measured) remain relatively constant with distance.

## 4.3. Ionization Parameter

Penston et al. (1990) demonstrated that the [O III]/[O II] line ratio is proportional to the ionization parameter  $U$  for radiation-bounded photoionized clouds irrespective of the shape of the ionizing continuum. Following Penston et al. (1990) we estimate the ionization parameter by the relationship:

$$U = 1.82 \times 10^{-3} [\text{O III}] \lambda 5007 / [\text{O II}] \lambda 3727 \quad (1)$$

where we use the reddening corrected ratio of [O III]  $\lambda 5007$  / [O II]  $\lambda 3727$ . Figure 9 shows the values of  $U$  plotted against the projected radius. Interpreted literally, this shows that the NW cone has slightly higher mean  $U$  than the SE cone, while the dust lane and outer regions of the cone have the lowest ionization parameter.

## 5. LINE RATIO DIAGRAMS

The utility of line diagnostic diagrams consisting of selected pairs of emission line ratios is well established. With such diagrams, different excitation mechanisms can be distinguished, chemical abundances may be estimated (in special circumstances), and physical parameters may be derived. The most commonly used diagrams involve ratios of bright, easily measured lines (Baldwin, Phillips

& Terlevich 1981), and the best of these restrict the choice of line ratios to emission lines that are close together in wavelength, avoiding the necessity to determine reddening corrections with great accuracy (Veilleux and Osterbrock 1987).

Our main objective in this section is to analyse the excitation mechanisms responsible for the emission lines. To do this we compare the observed line ratios with grids of shock and photoionization model predictions.

The models used here are:

- The MAPPINGS II shock and shock+precursor models of Dopita & Sutherland (1996). These models are parameterised by the shock velocity  $V_{shock}=200-500 \text{ km s}^{-1}$ , and the magnetic parameter  $B/n^{1/2} = 0-4 \mu\text{G cm}^{3/2}$ . In these models, EUV photons produced within the cooling region of the shock, diffuse both upstream and downstream. Those that go downstream are trapped by the shocked gas and produce a low-ionization parameter photoionized region near the point where hydrogen recombines. The combined spectrum of the cooling and photoionized gas we refer to as the “shock only” model. The (undoubtedly important) effect of thermal instabilities are not accounted for in this model. The photons which pass upstream produce a photoionized region of high ionization parameter and excitation in the pre-shock medium. The importance of this region depends upon whether this medium is able to absorb the ionizing photons. Shock models which include the contribution of both the shocked gas and its ionized precursor are referred to as “shock+precursor”.
- The power-law photoionization models presented in Allen, Dopita & Tsvetanov (1998). These are simplified photoionization models calculated with a ionizing spectrum of the form  $F_\nu \propto \nu^\alpha$ , with  $\alpha=-1, -1.4$  and  $-2$  and a range of ionization parameters ( $10^{-4} < U < 1$ ), and densities ( $100-1000 \text{ cm}^{-3}$ ). These models were calculated with the same MAPPINGS II code as the shock models described above.
- The  $A_{M/I}$  sequence of Binette, Wilson, & Storchi-Bergman (1996). This is a sequence of photoionization models which include both matter bounded and ionization bounded clouds, such that the ionizing spectrum incident on the ionization bounded clouds is filtered by the matter bounded component. Binette, Wilson, & Storchi-Bergman (1996) find that this two component model can account for some of the discrepancies of single component photoionization models. This sequence is parametrised by  $A_{M/I}$  which is the solid angle ratio of the matter bounded clouds to the ionization bounded clouds.

In plotting the observed points on the resulting line ratio diagrams, we maintain the same plotting point styles as used in section 3 to distinguish between the NW cone (open circles), SE cone (closed squares) and inter-cone (open triangles) regions. In each diagram we show the average error bar of the observed line ratio, and also provide an arrow indicating the direction of reddening correction. The shock model grids are labelled with the shock velocity and magnetic parameter.

The power-law photoionization  $U$  sequences are plotted for  $n = 100 \text{ cm}^{-3}$  and  $n = 1000 \text{ cm}^{-3}$  with grid lines of constant  $U$  every 0.25 dex. The  $A_{M/I}$  sequence is labelled with  $A_{M/I}$  and tick marks at intervals of 0.2 dex.

### 5.1. The Bright-line Diagnostic Plots

In Figures 10 through 16 we show the bright-line diagnostic plots which are generally used for determining excitation conditions in AGN. On these diagrams, we have sufficient observational points to analyse the detailed spatial structure of the ionization cones and the inter-cone region. In all of these diagrams the line ratios fall within limits that characterise Seyfert galaxies, in fact the points from this single object cover almost completely the regions of this diagram filled by samples of Seyfert galaxies (Veilleux and Osterbrock 1987), indicating that the NLR of NGC 2992 is characterized by a wide range of physical parameters. This is also reflected in the way that the points fall over a large  $U$  range of the parameter space covered by the various models.

In section 3 we have already shown how the [O III]  $\lambda 5007/\text{H}\beta$ , and [O III]  $\lambda 5007/\text{H}\alpha$  versus [N II]  $\lambda 6583/\text{H}\alpha$  diagrams separate the NLR of NGC 2992 into 3 distinct spatial regions. These diagrams are repeated here (Figures 10 and 11) with the model grids overlaid. Similar behaviour is clearly shown in other excitation-dependent diagnostic plots such as [O III]  $\lambda 5007/\text{H}\beta$  versus [S II]  $\lambda\lambda 6717,6731/\text{H}\alpha$  (Figure 12), or [O III]  $\lambda 5007/\text{H}\beta$  versus [O II]  $\lambda 3727/[\text{O III}] \lambda 5007$  (Figure 13), but is not apparent when the ratios of low-excitation lines with hydrogen are compared, such as the [N II]  $\lambda 6583/\text{H}\alpha$  and [S II]  $\lambda\lambda 6717,6731/\text{H}\alpha$  line ratios (Figure 14). In these diagrams the points from the different regions tend to cluster more tightly, and are not clearly separated as they are in Figures 10 and 11.

We will now consider how well the various theoretical sequences match (or do not match) the observations. First, the shock-only grid fails to match any of the observational data, for any of these diagnostic plots. Thus, if the ENLR gas is shock-excited, the shocks must be occurring in a matter-rich environment where the EUV photons produced by the shocks can be absorbed. We will not discuss the shock-only grids further.

The shock+precursor grids do much better. In all of the diagrams, with the exception of those which involve ratios of the [O I] lines, such as [O I]  $\lambda 6300/[\text{O III}] \lambda 5007$  (Figure 15), the observations define shock velocities which are reasonably consistent from one diagnostic diagram to another. For example, in Figures 10a, 11a and 12a the points from the NW and SE cones fall within the high shock velocity region ( $350\text{--}500 \text{ km s}^{-1}$ ) of the shock+precursor model grid. The inter-cone points show a large range in [O III]  $\lambda 5007/\text{H}\beta$  which extends these points along lines of decreasing shock velocity, down to as low as  $200 \text{ km s}^{-1}$  with approximately constant magnetic parameter in the shock+precursor model grid. However, the different diagnostic plots do not agree very well as to the value of the magnetic parameter, other than broadly excluding the possibility that this is less than about  $B/n^{1/2} \sim 1 \mu\text{G cm}^{3/2}$ . However, such scatter as is observed in this parameter between

the different diagrams can probably be ascribed to differences between the abundance set used in the models, and those that are applicable to NGC 2992, as well as to collisional de-excitation effects in the [O II] and [S II] lines, which are not modelled in these (low density limit) shock models.

Turning now to the simple photoionization models. In each of the diagnostic plots, the photoionization models overlap the same region of parameter space in this diagnostic diagram as the shock+precursor models, and so the observed points also fall within the photoionization  $U$ -sequences. However, different regions tend to be characterized by different ionization parameters and spectral index. For example, on Figure 10b, the NW cone points are within the  $\alpha = -1.4$  models with ionization parameter  $10^{-2.5} < U < 10^{-2.25}$ . The points from the SE cone show more scatter, but indicate an average ionization parameter which is lower than in the NW cone. Most of the SE cone points fall between the  $\alpha = -1.4$  and  $\alpha = -1.0$  sequences which may indicate a higher spectral index in the NW cone than in the SE cone. There is however a degree of degeneracy in the photoionization models such that increase in density or an increase in spectral index have a similar effect on the predicted line ratios.

The spread of the inter-cone points may therefore be partially explained by a wider range in density than we computed in the photoionization models. To investigate this possibility we extended the photoionization grid by calculating models with densities down to  $10^{-2} \text{ cm}^{-3}$ , for ionization parameters  $U = 10^{-2}$  and  $10^{-2.75}$ , and spectral index  $\alpha = -1.4$ . The low density limit occurs for density  $n_e \sim 1.0 \text{ cm}^{-3}$ , below which [O III]  $\lambda 5007/\text{H}\beta$  remains constant at  $\sim 10^{0.6}$  for  $U = 10^{-2}$  and  $\sim 10^{0.9}$  for  $U = 10^{-2.75}$ . However, the observed points extend over a wider range down to [O III]  $\lambda 5007/\text{H}\beta \sim 10^{0.3}$ , making it difficult to account for the observations with a photoionization models with a single value of the spectral index  $\alpha$  such as would be required in a self-consistent photoionization model of the whole NLR.

Different diagnostic plots yield different estimates for both  $\alpha$  and for  $U$ . For example, the NW cone points that fall within the  $\alpha = -1.4$   $U$ -sequence in Figures 10b and 11b, are shifted closer to the  $\alpha = -1$   $U$ -sequences in Figure 12b, with a lower value of  $U$ . The shift of the points with respect to the photoionization  $U$ -sequences is significant, being approximately 4 times the average  $1\sigma$  error bar of the [S II]  $\lambda\lambda 6717, 6731/\text{H}\alpha$  observations. For the [S III]  $\lambda\lambda 9069, 9532/\text{H}\alpha$  versus [S II]  $\lambda\lambda 6717, 6731/\text{H}\alpha$  plot (Figure 16),  $\alpha \sim -2$  is indicated. In general, most of the plots are consistent with  $U \sim 10^{-2.5}$  for the bright parts of the cones, but those involving [N II]  $\lambda 6583 / \text{H}\alpha$  versus [S II]  $\lambda\lambda 6717, 6731/\text{H}\alpha$ , and [S III]  $\lambda\lambda 9069, 9532/\text{H}\alpha$  versus [S II]  $\lambda\lambda 6717, 6731/\text{H}\alpha$  are more consistent with  $U \sim 10^{-4}$ .

We can therefore conclude that not only are the observations inconsistent with a single value of  $\alpha$  within individual line ratio diagrams, but also that different diagnostic diagrams do not furnish consistent values of  $\alpha$  between one another. Since photoionization models should be characterised by a unique value of  $\alpha$  determined by the intrinsic nuclear spectrum (although  $U$  may change from one region to another), these observations provide a serious challenge to photoionization modellers.

By contrast, the shock+precursor models indicate values of the shock velocity which are con-

sistent from one diagram to another; of order 350–500 km s<sup>-1</sup> in the cones, falling to as low as 200 km s<sup>-1</sup> in the inter-cone region. In the shock+precursor picture, the apparent changes in both  $\alpha$  and  $U$  according to the photoionization interpretation is the result of changes in the spectral energy distribution and the total energy flux in the ionizing radiation as a function of shock velocity.

These problems with photoionization models are not resolved by use of the  $A_{M/I}$  sequence. Indeed, the fact that  $A_{M/I}$  sequences are very similar to  $U$ -sequences, when plotted on the traditional line ratio diagrams was shown in Binette, Wilson, & Storchi-Bergman (1996). This is apparent in Figures 10b, and 11b where the  $A_{M/I}$  sequence is very close to the higher density  $\alpha=1.4$   $U$ -sequence. With respect to the  $A_{M/I}$  sequence, the observed points from the SE and NW cones shown in Figures 10b and 11b cluster around the sequence for values of  $A_{M/I}$  in the range  $1 \lesssim A_{M/I} \lesssim 6$ . The SE cone points tend to have [O III]  $\lambda 5007/H\beta$  higher than the  $A_{M/I}$  sequence prediction, while the NW cone points have [O III]  $\lambda 5007/H\beta$  slightly lower than the  $A_{M/I}$  sequence, and favour higher values of  $A_{M/I}$ . As with the  $U$ -sequences, the inter-cone points tend to diverge from the  $A_{M/I}$  sequence. In general the  $A_{M/I}$  sequences can neither explain the range or the direction of scatter of the observations in NGC 2992. In addition, in some cases such as in the [N II]  $\lambda 6583/H\alpha$  versus [S II]  $\lambda\lambda 6717,6731/H\alpha$  and the [S III]  $\lambda\lambda 9069,9532/H\alpha$  versus [S II]  $\lambda\lambda 6717,6731/H\alpha$  diagrams (Figures 14 and 16 respectively), the  $A_{M/I}$  sequence is offset from the observations by an amount which is larger than could be explained by abundance variations.

The result of comparing the ratios of the bright lines mapped over the NLR of NGC 2992 can be summarized as follows: The ratios of [O III], [N II], [S II] and [S III] generally fall within the parameter space covered by both the shock+precursor, and photoionization  $U$ -sequence models. The ratios of these lines fall consistently in the same location of the diagnostic diagrams relative to the shock+precursor grid, but do not provide consistency with respect to the photoionization models. [O II] appears to be slightly overestimated in both shock+precursor and photoionization models, and [O I] is predicted to be too strong in all the models.

## 5.2. Faint line diagnostic diagrams

The lines of [Ne V]  $\lambda 3426$ , He II  $\lambda 4686$  and [O III]  $\lambda 4363$  also are important diagnostics, but are relatively faint lines so we are not able to spatially map them over the entire ENLR of NGC 2992. In the following three diagrams we compare the model predictions with the observations of these lines in the average spectra of the NW and SE cones.

Figure 17 shows [S II]  $\lambda\lambda 6717,6731/H\alpha$  versus He II  $\lambda 4686/H\beta$ . In this diagram the shock-only and shock+precursor models overlap, so we show the shock-only model grid with dashed lines. It is clear from this diagram that the He II  $\lambda 4686/H\beta$  ratio is underestimated in the shock+precursor models but the photoionization  $U$ -sequence shown in Figure 17b can account for the large He II  $\lambda 4686/H\beta$  ratio with  $\alpha = -1$  and ionization parameter  $10^{-3} < U < 10^{-2}$ .

The line ratios used in Figure 17 are identified by Binette, Wilson, & Storchi-Bergman (1996)



as one of the combinations for which  $A_{M/I}$  and  $U$ -sequences show markedly different behaviour. This is apparent in Figure 17b where the  $A_{M/I}$  sequence cuts across the  $U$ -sequences curves. The data points for the NW and SE cones fall relatively close to the  $A_{M/I}$  sequence for  $A_{M/I} \sim 1$ .

Figure 18 shows He II  $\lambda 4686/H\beta$  with [O II]  $\lambda 3727/[O III] \lambda 5007$ , where we have plotted the shock models, photoionization models and  $A_{M/I}$  sequence on the one diagram. The relative positions of the various grids in this diagram are similar to those Figure 17, and we find that the points fall in similar positions with respect to the  $A_{M/I}$  sequence and  $U$ -sequences, but fall well off the shock and shock+precursor grids.

Figure 19 combines the ratio of the high excitation [Ne V]  $\lambda 3426$  line to [Ne III]  $\lambda 3869$  versus the [O III]  $\lambda 5007/H\beta$  ratio. The data points from the SE and NW cones fall approximately  $3\sigma$  to the right of the shock+precursor models, but do fall within the  $\alpha = -1$  photoionization model. The inferred ionization parameter from the position of the data points on the  $U$ -sequences is much higher than inferred from the other diagrams, however the fact that the  $U$ -sequences fold over themselves in this region of the diagram (causing some regions to have double valued solutions within the photoionization models) makes this inference very uncertain. The  $A_{M/I}$  sequence again shows different behaviour to the  $U$ -sequences and the data points fall near the  $A_{M/I} \sim 0.6$  prediction.

Shock models of this simple class are known not to provide a good description of the very high-excitation line spectrum. This includes the He II and [Ne V] lines as well as higher excitation species such as [Fe VII]. These lines are better predicted by models which include a component of optically thin gas with high ionization parameter. The  $A_{M/I}$  sequence is an example this. The two components used in the  $A_{M/I}$  models can be considered to be a simple approximation of an inhomogeneous medium which may contain regions of different optical thickness to ionizing radiation. The success of the  $A_{M/I}$  sequence in predicting the line ratios as shown in the faint-line diagnostic diagrams may attest to the presence of inhomogeneities in the ionized clouds. The ionized precursor gas in our shock+precursor models is homogeneous and is thus not expected to reproduce these lines accurately. Nevertheless, Dopita (1997) has shown that an optically thin, high ionization parameter component which emits high ionization lines, can be produced in the context of more complex shock models associated with shocked entrainment layers at the boundary of ionization cones.

It may also be possible for combined shock and central source photoionization models to provide a better match to the observed line ratios. Such models are however difficult to constrain and we find no obvious spatial or spectral separation of shock and central source components in our data, so we have not attempted a combined model. Nevertheless it is clear that these diagnostics involving faint high excitation lines will be very useful in developing more sophisticated models of shocks, photoionization or combinations of shocks and central source photoionization.

### 5.3. The temperature sensitive diagnostic diagram

A long-standing problem in AGN modelling has been the so-called temperature problem. Briefly the nature of this problem is that simple photoionization models give low temperatures (less than 15000 K), which disagrees with observations of [O III]  $\lambda 4363$ /[O III]  $\lambda 5007$  in NLRs of some active galaxies, for which the inferred electron temperatures range up to  $\sim 22000$  K (Tadhunter, Robinson & Morganti 1989). Shocks can better account for the high temperatures because the [O III]  $\lambda 4363$  emission from shocks is dominated by the 40000-20000 K region of the cooling zone behind the shock front (Dopita & Sutherland 1995). Recently Binette, Wilson, & Storchi-Bergman (1996) have shown the  $A_{M/I}$  models can also predict high values of [O III]  $\lambda 4363$ /[O III]  $\lambda 5007$ . Also some of the earlier [O III]  $\lambda 4363$  line measurements may be overestimated due to poor subtraction of the underlying galaxy spectrum. We now compare the temperature sensitive line ratios observed in NGC 2992 to the model predictions.

Figure 20 employs the temperature sensitive ratio of [O III]  $\lambda 4363$ /[O III]  $\lambda 5007$  on the y-axis, versus He II  $\lambda 4686$ /H $\beta$  on the x-axis. Due to the different temperature regimes of the shock and photoionization models, the grids are widely spaced in this diagram. A temperature axis is plotted on the left side of the diagram showing the inferred temperatures calculated from the [O III]  $\lambda 4363$ /[O III]  $\lambda 5007$  ratio in the same manner as discussed in section 4.1.

The large [O III]  $\lambda 4363$ /[O III]  $\lambda 5007$  values predicted by the shock-only model reflect the high temperatures that occur in the cooling region behind the shock front. The photoionization model grids display the well known result that  $U$ -sequences generally have [O III] temperatures less than 15000 K. The highest [O III] temperatures obtained in photoionization models occur for the  $\alpha = -1$  model with ionization parameter  $U = 0.1$ , with the  $A_{M/I}$  able to produce a similarly high [O III] temperature. As shown in section 4.1 the average spectra of the NW and SE cones have [O III] temperatures of 14780 K and 16990 K respectively. The location of the data points on this temperature axis are consistent within the error bars with the [O III] temperatures predicted by the shock models, the  $A_{M/I}$  sequence and also the  $\alpha=-1$ ,  $U=0.1$  photoionization models.

Binette, Wilson, & Storchi-Bergman (1996) show that high temperatures are obtained in the  $A_{M/I}$  sequence because the MB component is chosen to be sufficiently thin that the temperature is governed by the photoionization of He $^+$ , and that the O $^{+2}$  zone is truncated before the internal temperature of that zone falls enough to decrease the [O III]  $\lambda 4363$ /[O III]  $\lambda 5007$  ratio. The  $A_{M/I}$  sequences described by Binette, Wilson, & Storchi-Bergman (1996) (and displayed in Figure 12 of Binette, Wilson, & Storchi-Bergman 1996) can reach [O III]  $\lambda 4363$ /[O III]  $\lambda 5007 \sim 0.019$  for an incident  $\alpha = -1.3$  ionizing spectrum (as plotted in Figure 20), up to  $\sim 0.025$  for an incident ionizing spectrum with  $\alpha = -1.1$ , and as high as  $\sim 0.048$  when the metallicity of the gas is decreased to  $Z=0.2$ . As such these  $A_{M/I}$  sequences are able to reproduce the relatively high temperatures observed in the NW and SE cones of NGC 2992.

## 6. CENTRAL SOURCE TEST

### 6.1. Determination of $Q$ from [S II] density.

Metz et al. (1996) describe a method to test whether the line emitting gas in the NLRs of Seyfert galaxies is photoionized by a central source. The test uses the definition of the ionization parameter for radiation from a central source incident on an emission line cloud:

$$U = \frac{q}{n_e r^2 c} > \frac{q}{n_e (r / \cos \theta)} \quad (2)$$

where  $q$  is the number of ionizing photons per unit time per steradian,  $n_e$  is the electron density, and  $r$  is the distance of the emission line cloud from the source.  $\theta$  is the angle between a line from the source to the cloud and the plane of the sky. Using [O III]  $\lambda 5007$ /[O II]  $\lambda 3727$  to estimate  $U$ , [S II]  $\lambda 6717$ / $\lambda 6731$  to measure the density  $n_e$  and estimating  $r$ , allows  $q$  to be determined. If the assumption of a central source is correct, then  $q$  should be independent of position in the NLR. Using long slit spectroscopy Metz et al. (1996) applied this technique to the NLR of three nearby Seyfert galaxies including NGC 2992. In the case of NGC 2992 their slit was aligned along the radio structure (PA = 26°). They find that  $q$  rises with increasing distance from the nucleus in all three NLR.

Here we perform a similar test on NGC 2992 using our data which has more complete spatial coverage of the NLR than the single slit in Metz et al. (1996). We confirm the result that  $q$  measured in this way does rise with increasing distance from the nucleus. However we find that the [S II]  $\lambda 6717$ / $\lambda 6731$  density diagnostic is not sensitive in the density range required to measure  $q$  in the NLR of NGC 2992, and thus demonstrate that the test is invalid.

To perform the “ $q$ -test” with our spectra of NGC 2992 we have considered only the regions within the bi-cone of opening angle 116° centred on the nucleus in which have well determined [S II] density measurements.  $U$  is determined by using the reddening corrected [O III]  $\lambda 5007$ /[O II]  $\lambda 3727$  ratio as described in section 4.3. The values of  $n_e$  and  $U$  for points within the cone are shown in Figures 21a and 21b respectively. To estimate the de-projected distances of points in the bi-cone to the nucleus, we have considered all the points to lie within the geometric volume of the bi-cone. Narrow band images show that the bi-cone axis is aligned at roughly right angles to the plane of the galaxy. Here we assume that the bi-cone has the same inclination on the sky as the galaxy, and that the SE cone is the near one. Using this geometry we can then calculate two values for the de-projected radius of each point <sup>3</sup>, which correspond to the near and far surfaces of the cones.

---

<sup>3</sup>

$$r_{deprojected} = \frac{y(\cos(\psi + i) + \sin \psi \sin i) \pm \sqrt{y^2 \sin^2 \psi \sin^2 i - x^2 \sin^2 i \cos^2(\psi + i) - 2x^2 \cos(\psi + i) \sin \psi \sin^3 i}}{\cos^2(\psi + i) + 2 \cos(\psi + i) \sin \psi \sin i} \quad (3)$$

where  $i$  is the angle subtended by the cone axis to the plane of the sky, and  $\psi$  is the half angle of the cone.

These two values represent the extrema for the de-projected radii of points within the cones, and we calculate  $q$  using both values, and likewise with the projected radius.

The diagrams on the left hand side of Figure 22 show the values of  $Q = 4\pi q$  derived for; (i) de-projection onto the near side for both cones (top panel), (ii) de-projection onto the far side of the cones (middle panel) and (iii) no de-projection (bottom panel). In all cases  $Q$  is found to rise with increasing distance from the nucleus, and the result is relatively insensitive to the de-projection used.

A rising  $Q$  is inconsistent with photoionization from the central nucleus, because in this case  $Q$  should have the same value wherever it is measured. Metz et al. (1996) rule out the possibility that this result is due to a projection effect because it would require  $\theta$  to increase towards the nucleus, which is inconsistent with the observed sharp edged shape of the cone. Metz et al. (1996) also note that a two-component ionizing continuum due to a mixture of ionization bounded and matter bounded clouds cannot account for the observed increase in  $Q$ . Although photoionizing shocks (Dopita & Sutherland 1995) provide a local source of UV which might explain the rising trend of  $Q$ , it is more likely that the apparent increase in  $Q$  is spurious, and is the result of overestimating the average density using the [S II]  $\lambda 6717/\lambda 6731$  ratio.

The [S II]  $\lambda 6717/\lambda 6731$  ratio is only sensitive as a density diagnostic over the range  $\sim 100\text{--}10000$   $\text{cm}^{-3}$ . The ratio tends to a limit of 1.4 for lower densities, and 0.44 for higher densities. In NGC 2992 we find that the [S II] density for some locations near the nucleus is in the range  $100\text{--}400$   $\text{cm}^{-3}$ , however for many locations the [S II]  $\lambda 6717/\lambda 6731$  ratio lies near or below the lower limit of the usable range of this density diagnostic. If we take the value of  $Q$  as measured near the nucleus where the density is relatively well determined, we find  $Q = 10^{52.9}$ , in units of photons  $\text{s}^{-1}$ . This value is probably reliable, and reflects the true value for the central ionizing source. Using this value of  $Q$ , and the measurements of the ionization parameter and de-projected distances, we rearrange equation 2 to calculate the density required at each location,  $n_{e,Q}$ , to keep  $Q$  constant:

$$\log(n_{e,Q}) = \log(52.9) - \log(4\pi c) - \log U - 2 \log r \quad (4)$$

The diagrams on the right hand side of Figure 22 show the results of this calculation, with  $\log n_{e,Q}$  plotted against  $r$  for each of the de-projections. The dashed line indicates the lower useful limit for the [S II] density diagnostic. Most of the points indicate that  $n_{e,Q}$  is below this limit. Thus if  $Q$  is actually constant at  $10^{52.9}$  photons  $\text{s}^{-1}$ , we would not be able to measure it at large  $r$  because the density diagnostic is not sensitive in the range required. The  $q$ -test is therefore invalid in this case. However, if the local density is really as high as  $200\text{--}300$   $\text{cm}^{-3}$  in the regions at large  $r$  where we can measure it, then we would still require shocks if only to produce a local compression.

## 6.2. Determination of $Q$ from the $H\alpha$ luminosity

In this section we compute the rate of hydrogen recombinations  $Q_{rec}$  from the  $H\alpha$  luminosity and compare this to the rate of ionizing photons  $Q$ , derived from the emission line ratios above. In photoionization equilibrium the rate of hydrogen recombinations must equal the rate of ionizing photons. The rate of hydrogen recombinations  $Q_{rec}$  can be derived from the  $H\alpha$  luminosity by comparing the effective recombination coefficient to produce  $H\alpha$  photons with the total (Case B) recombination coefficient for hydrogen:

$$Q_{rec} \simeq 1.39 \times 10^{52} L_{40}(H\alpha) \text{ photons s}^{-1} \quad (5)$$

where  $L_{40}(H\alpha)$  is the  $H\alpha$  luminosity (in units of  $10^{40}$  ergs  $s^{-1}$ ). In the case where a central source is illuminating the NLR:

$$Q_{rec} \simeq 1.39 \times 10^{52} L_{40}(H\alpha) \frac{4\pi}{\epsilon\omega} \text{ photons s}^{-1} \quad (6)$$

where  $\epsilon$  is the fraction of ionizing photons that are absorbed, and  $\omega$  is the solid angle subtended by the  $H\alpha$  emitting region as seen from the nucleus.

The reddening corrected  $H\alpha$  luminosities of the NW and SE cones are estimated from our  $H\alpha$ + $[N\ II]$  narrow band image, corrected for reddening with a reddening map derived from the grid of  $H\alpha/H\beta$  ratios measured from the spectra. The reddening map was constructed by re-sampling the semi-regularly spaced grid of reddening constants from the spectra onto the image pixel grid with the IDL *TRIGRID* routine. The  $H\alpha$ + $[N\ II]$  flux is summed over the specified region in the reddening corrected image, and a correction applied for the  $[N\ II]$  contribution using the average  $[N\ II]/H\alpha$  ratio of the region as measured from the spectra. This yields the total  $H\alpha$  flux which is then converted to a luminosity using the distance to NGC 2992 (30.8 Mpc). For each of the SE and NW cones, we have used only the  $H\alpha$  luminosity of the cones (corresponding to the same region over which  $Q$  is calculated in the previous section) and have specified  $\omega = 2.26$  steradian, the solid angle of the cone subtended at the nucleus. The calculation of  $Q_{rec}$  for the entire NLR region ignores the cone geometry and uses the total  $H\alpha$  luminosity and  $\omega = 4\pi$ . The dominant source of uncertainty in these calculations are errors in the reddening correction, and the implicit assumption that  $\epsilon$  is unity. This means that the  $Q_{rec}$  values derived represent a lower limit estimate of the number of ionizing photons  $Q$ .

The values of  $L_{40}(H\alpha)$  and  $Q_{rec}$  computed for the NW and SE cones, and the NLR as a whole are shown in table 2<sup>4</sup>. Comparing  $Q_{rec}$  derived from the  $H\alpha$  luminosity, and the  $Q$  derived from the forbidden emission line ratios we find that  $Q_{rec}$  lies within the computed range of the  $Q$  values for all the regions considered. If the whole region was photoionized by a single central source then we

---

<sup>4</sup>Table 2 also contains  $L_{40}([O\ III])$  calculated from the reddening corrected  $[O\ III]$  narrow band image

should expect the values of  $Q_{rec}$  to correspond to the value of  $Q$  as determined for the inner parts of the NLR in the previous section. However, our lower limits for  $Q_{rec}$  are however consistently higher than the value of  $Q$  derived at the inner edge of the NLR ( $10^{52.9}$  photons  $s^{-1}$ ).

In conclusion, although the  $q$ -test in its original form is invalid, there does appear to be real evidence for a local source of ionizing photons with a hard spectrum within the cone. This can only come from photoionizing shocks. We note that a method along the lines of the  $q$ -test as described here, but devoid of the density diagnostic limitations, to quantify the relative contributions to the ionizing field from local and central sources. This would aid the development of combined shock and central source photoionization models.

## 7. SHOCK ENERGETICS

The emission line properties of the ENLR of NGC 2992 appear to be understandable in the context of shock excitation of the gas. In this section we compare the excitation of the gas to the kinematics of the outflow/wind, and also compare the energetics of the radio and X-ray plasma to the emission line gas.

### 7.1. Excitation and Kinematics

As described in section 1, the kinematics of the emission line gas shows a outflow velocity field superimposed on the underlying galaxian rotation. Figure 23a shows a map of the the velocity difference of the wind component to the galaxy rotation from our high resolution spectra of the [O III] line. The wind component is systematically blueshifted in the SE cone, and redshifted in the NW cone with velocities of up to  $\sim 200$  km  $s^{-1}$ . A map of the FWHM of the wind component shown in Figure 23b reveals that the SE cone has the broader FWHM, and we consider this to be evidence of greater dynamical activity in the SE cone.

If shocks are important for the excitation of the gas, we may expect the kinematical properties of the gas to in some way correlate with excitation. To compare the excitation of the gas with the kinematics we re-binned the high and low resolution spectra onto a common spatial grid covering the ENLR, and extracted the emission line ratios, and kinematical properties at each grid point. We now compare the [O III]  $\lambda 5007/H\beta$ , and [N II]  $\lambda 6583/H\alpha$  ratios to the kinematics.

In Figure 24a we plot the [O III]  $\lambda 5007/H\beta$  ratio, which is a measure of the excitation of the gas, versus the FWHM of the kinematical components. The kinematical component identified with the galaxy rotation are plotted as the solid circles, the main outflow components (as shown in Figure 23) are plotted as open squares and where the extra component is detected (at a few locations), this is plotted as open triangles. The uncertainty in the FWHM is generally less than 100 km  $s^{-1}$ .

The outflow component points show a wide range in FWHM from 100 to 670 km s<sup>-1</sup>, whereas the FWHM of the rotational component is much more quiescent, and is generally less than ~200 km s<sup>-1</sup>. The excitation of the rotational component covers the full range in [O III]  $\lambda$ 5007/H $\beta$ , while the wind components tend to show higher [O III]  $\lambda$ 5007/H $\beta$  ratios in locations where the lines are wider. No regions with line FWHM > 250 km s<sup>-1</sup> display low excitation.

We also compare the data points on the excitation versus line width diagram to the theoretical curves predicted by the shock+precursor models. The solid curve assumes the FWHM is directly related to the shock velocity, and the dashed curve assumes that the FWHM is associated with the projection of randomly oriented shocks so that  $V_{shock} \simeq \text{FWHM}/\sqrt{3}$ . While the spread of the observed points is very suggestive of shock activity, it is not what would be expected for a simple shock moving into an undisturbed pre-shock medium. In this case, the regions of very high [O III]  $\lambda$ 5007/H $\beta$  ratio would arise in the precursor, which would be kinematically undisturbed, and therefore there would be an inverse correlation of line width and excitation. However, if the shocks arise in a mass-entraining flow, the strong shocks are located near the outer boundary of the entrainment flow, and the photoionized precursor medium is the fast-moving material inside this (Dopita 1997). This geometry would provide the direct correlation between line width and excitation observed.

In Figure 24b we plot the [N II]  $\lambda$ 6583/H $\alpha$  ratio versus the FWHM of the outflow components. As in Figure 24a the square points indicate the main outflow component, and the triangles indicate the extra component. Here we make the distinction between the cones by using filled symbols for the SE cone and open symbols for the NW cone. The cones are clearly separated in Figure 24b because the NW cone has lower [N II]  $\lambda$ 6583/H $\alpha$  and lower FWHM, while the more dynamically active SE cone has higher [N II]  $\lambda$ 6583/H $\alpha$ . The shock+precursor curves plotted on Figure 24b show that the models predict higher [N II]  $\lambda$ 6583/H $\alpha$  for faster shock velocities. This suggests that the higher [N II]  $\lambda$ 6583/H $\alpha$  in the SE cone is directly related to the greater dynamical activity in that cone.

The difference in shock velocity between the cones inferred from these curves is however greater than that indicated by the [O III]  $\lambda$ 5007/H $\beta$  ratio which indicates only slightly faster average shock velocity in the SE cone (see Figure 10a). As such, the increase in [N II]  $\lambda$ 6583/H $\alpha$  is likely due to a combination of faster shock velocity and increased magnetic parameter, both of which may be expected in the more turbulent conditions within the SE cone.

## 7.2. Thermal pressure energy source for the ENLR

Another aspect of shock energetics is related to the question of whether there is sufficient energy in the radio plasma to power the optical emission. For Seyferts, classical equipartition arguments suggest that the pressure in the relativistic plasma is inadequate to drive high velocity shocks into the interstellar medium and produce the observed emission line flux (Wilson, Ward, &

Haniff 1988). Recently Bicknell et al. (1998) have argued that the radio plasma may only trace a fraction of the available energy which exists in an entrained thermal phase, which is not detected in synchrotron emission, and that the NLR may well be powered by the energy and momentum flux originally carried by the radio-emitting jets.

Briefly summarising the physics detailed in Bicknell et al. (1998): The total energy of a jet-fed lobe is  $f_{ad}F_E t$  where  $F_E$  is the jet energy flux,  $t$  is the age of the lobe and  $f_{ad} \sim 0.5$  is a factor which accounts for energy lost in adiabatic expansion. Expansion of the lobe gives rise to narrow line emission via shocks and the jet energy flux  $F_E$  can be estimated from the [O III]  $\lambda 5007$  luminosity,  $L([\text{O III}]) \sim 0.01 F_E$ . The relativistic electrons in the lobe emit radio wavelength synchrotron radiation, and the ratio of the monochromatic radio power of the lobe (in synchrotron radiation) to the jet energy flux can be expressed as:

$$\kappa_\nu \simeq C(a)B^{(a+1)/2}\nu^{-(a-1)/2}f_e f_{ad}t \quad (7)$$

where  $a$  is the power-law exponent of the electron energy distribution,  $C(a)$  depends on synchrotron parameters, and  $B$  is the randomly oriented magnetic field.  $f_e$  is the fraction of the total energy in relativistic electrons and positrons, and is thus a measure of non-thermal to thermal composition of the plasma. We now use the relationships detailed in Bicknell et al. (1998) to investigate the possibility of a thermal energy source for the ENLR of NGC 2992.

Our reddening corrected [O III]  $\lambda 5007$  luminosity gives an estimate of  $F_E = 9.6 \times 10^{43}$  ergs  $s^{-1}$ , and the 335 mJy flux density detected in the Fleurs map of Ward et al. (1980) gives a radio power at 1.4 GHz of  $P_{1.4} = 3.8 \times 10^{29}$  ergs  $s^{-1}$   $\text{Hz}^{-1}$ . This yields  $\kappa_{1.4} = 4 \times 10^{-15}$   $\text{Hz}^{-1}$ , which is typical of Seyfert galaxies (eg. Bicknell et al. 1998).

The total pressure can be expressed as:

$$P_{tot} = P_{particles} + B^2/8\pi \quad (8)$$

where

$$P_{particles} = P_e + P_{th} = (1 + k)P_e \quad (9)$$

is the total pressure in relativistic electrons  $P_e$  plus the pressure in thermal particles  $P_{th}$ .

The minimum pressure magnetic field is obtained by minimising the total pressure subject to the constraint of the observed radio surface brightness. Normally when estimating the pressure in the plasma of radio galaxies via minimum pressure arguments, one takes  $k \sim 1$ . For NGC 2992, using  $k = 1$ , an assumed spectral index of 0.7 and an electron index  $a = 2.4$  we obtain  $P_{particles} = 1.1 \times 10^{-11}$  dyn  $\text{cm}^{-2}$ , and a minimum pressure magnetic field of  $B = 1.5 \times 10^{-5}$  G. Colbert et al. (1998) infer the pressure of the X-ray gas to be  $1.9 \times 10^{-11}$  dyn  $\text{cm}^{-2}$  for  $T=0.1$  keV, and  $7.9 \times 10^{-11}$  dyn  $\text{cm}^{-2}$  for  $T=1$  keV. This is larger than the value for  $P_{particles}$  obtained in the minimum pressure calculation with  $k = 1$ , although only marginally so for  $T=0.1$  keV. Therefore



it is possible that the conventional estimate of the minimum pressure associated with the non-thermal plasma is an underestimate. Moreover, we note that in order to drive a shock with velocity  $\sim 350 \text{ km s}^{-1}$  into gas with a pre-shock number density of  $\sim 1 \text{ cm}^{-3}$ , we require a pressure of  $\sim 10^{-9} \text{ dyn cm}^{-2}$ . This is well above the upper X-ray estimate, although the latter is based upon the total extended X-ray luminosity and is therefore an average. Nevertheless the point remains that the pressure of the X-ray emitting gas is possibly well above the conventionally calculated non-thermal value.

Therefore we consider values of the parameter  $k \gg 1$ . We find that the thermal pressure,  $\frac{k}{1+k}P_{particles}$ , is equal to upper value for the pressure in the X-ray gas for  $k = 75$ . The minimum pressure magnetic field in this case is  $B = 4.1 \times 10^{-5} \text{ G}$ . If the lower X-ray pressure is relevant, we obtain values of  $k = 6$  and  $B = 2.2 \times 10^{-5} \text{ G}$ ; that are close to the minimum pressure values for the  $k = 1$  case.

Using these values of  $k$  we now estimate  $f_e$ :

$$f_e \equiv \frac{\epsilon_e}{\epsilon_e + \epsilon_{th}} = [1 + (P_{th}/2P_e)]^{-1} = [1 + k/2]^{-1} \quad (10)$$

where  $\epsilon_e$  and  $\epsilon_{th}$  are the energy densities of the relativistic and thermal components. This gives  $f_e=0.026$  for  $k = 75$ , and  $f_e=0.25$  for  $k = 6$ . These low values of  $f_e$ , in particular  $f_e=0.026$ , indicate that the relativistic gas which is responsible for the radio emission may constitute only a small fraction of the total energy.

Estimating the age to be  $t = 10^6 - 10^7$  yrs from the expansion time-scale, and  $f_{ad} \sim 0.5$ , we obtain  $\tau = f_e f_{ad} t = 10^{4.1} - 10^{5.1}$  yrs for  $f_e=0.026$ , and  $\tau = 10^{5.1} - 10^{6.1}$  yrs for  $f_e=0.25$ . Using these values of  $\tau$  and the corresponding minimum pressure magnetic fields we can read off  $\kappa_{1.4}$  from Figure 2 in Bicknell et al. (1998). This gives  $\kappa_{1.4}$  in the range  $2 \times 10^{-14} - 7 \times 10^{-13} \text{ Hz}^{-1}$ . These values are larger than the observed value of  $\kappa_{1.4}$  described above, implying that the energy associated with the radio and X-ray gas is less than the amount required to power the total optical emission of the ENLR. Given the uncertainties in the X-ray images and the reddening correction to the [O III]  $\lambda 5007$  luminosity, we may view the results presented here as accurate to an order of magnitude. Even so, this result represents a significant difference compared to the traditional value of  $\kappa_{1.4} \approx 10^{-11}$  which is implicitly used when the radio emission is considered as a scaled down version of a radio galaxy lobe.

Another possibility is that minimum pressure conditions are not appropriate. In this case, with  $k = 1$ , the magnetic field required for the total particle pressure to equal the X-ray gas pressure is  $B = 3.3 \times 10^{-6} \text{ G}$  for the upper value of the X-ray gas pressure, and  $B = 7.5 \times 10^{-6} \text{ G}$  for the lower value of the X-ray pressure. Using the same estimates for  $t$  and  $f_{ad}$  as above leads to estimates of  $\kappa_{1.4} = 5 \times 10^{-15} - 6 \times 10^{-14} \text{ Hz}^{-1}$  for the upper value of the X-ray pressure and  $\kappa_{1.4} = 3 \times 10^{-14} - 3 \times 10^{-13} \text{ Hz}^{-1}$  for the lower value of the X-ray pressure. The observed value of  $\kappa_{1.4}$  is outside of these ranges, but only marginally so for the upper value of the X-ray pressure.

In the context of the theoretical work of Bicknell et al. (1998) the properties of the optical, radio and X-ray emitting gas in NGC 2992 indicate that the energy associated with the radio plasma and the X-ray emitting gas may provide a larger fraction of the energy required to power the ENLR than anticipated by previous calculations for Seyferts which assume  $\kappa_{1.4} = 3 \times 10^{-11}$ . The uncertainties in the above calculations could be reduced if an accurate estimate of the temperature of the X-ray emitting gas was available.

## 8. CONCLUSIONS

The physical properties of NGC 2992 derived from the emission line spectra show that the ENLR is characterized by relatively high temperature, [S II] densities up to  $400 \text{ cm}^{-3}$  and a fairly wide range of excitation.

In comparing the spatially mapped line ratios with an extensive shock and photoionization model grids, we have shown that the observations generally fall within the parameter space defined by either class of model. However, in terms of the consistency of the model predictions from one diagnostic diagram to another, the shock+precursor models provide a better outcome. The ionization cones are characterised by a shock velocity of  $350\text{--}500 \text{ km s}^{-1}$ , consistent with the line widths found in high resolution observations. In the inter-cone region, and about the edges of the ionization cones, the velocities inferred are lower, ranging down to about  $200 \text{ km s}^{-1}$ . Single component photoionization models would require a range of spectral indices in the different regions, which is not allowed in a model where the photons are provided by a central source. In addition, different line ratios demand different values of the ionization parameter in the same region, which is again inconsistent. The two component  $A_{M/I}$  sequence model of Binette, Wilson, & Storchi-Bergman (1996) is generally better able to account for the observed line ratios than the simple single component photoionization models. Indeed, the fit provided by both the shock and photoionization hypotheses, in particular for the higher ionization lines, would be improved by more sophisticated multi-component models.

We have applied the  $q$ -test for a central ionizing source and have shown that the apparent increase in the rate of ionizing photons,  $q$ , with distance from the nucleus is most likely due to overestimation of the average density with the [S II]  $\lambda 6717/\lambda 6731$  ratio. The most reliable values of  $q$  determined at the inner edge of the NLR, are however below the lower limits for the hydrogen recombination rate  $Q_{rec}$  suggesting that there is a source of locally produced ionizing photons which may be attributed to the ionizing field generated by fast shocks.

Despite the lack of any direct morphological indication of interaction between the radio or X-ray plasma with the emission line gas in NGC 2992, shocks must play an important role in this object. The outflow kinematics attest to this, because strong shocks with Mach numbers of order 40 simply must occur in such dynamically active gas. Furthermore, the observation of co-spatial X-ray and radio emitting plasma support the entrainment theory of Bicknell et al. (1998) in which

the Seyfert jets are dominated by the entrained thermal plasma. In this object we find that the energy associated with the radio and X-ray plasma may account for a large fraction of the energy required to power the total optical emission of the ENLR.

While the emission line ratios alone cannot uniquely determine shocks as the dominant excitation mechanism, the observed ratios and the velocity field and the kinematical line widths are all broadly consistent with shocks, and with the energetics as determined from the radio and X-ray plasma.

We find no spectral evidence for significant contribution to the ionizing field or outflow from a starburst component, and favour the interpretation of Colbert et al. (1998) that the source of the outflow is an initially relativistic jet originating at the AGN.

We thank Geoff Bicknell for assistance with the energy budget calculations in this paper, and for the use of his minimum pressure program. MA acknowledges the support of an APRA scholarship. We are grateful for an Australian DIST International Science and Technology Major Grant which facilitated the cooperation between MSSSO and The Johns Hopkins University. This research has made use of the NASA/IPAC Extragalactic Database (NED), which is operated by the Jet Propulsion Laboratory, Caltech, under contract with NASA.

## REFERENCES

- Allen, M. G., Dopita, M. A., & Tsvetanov, Z. I. 1998, *ApJ*, 493, 571
- Antonucci, R. R. J. & Miller, J. S. 1985, *ApJ*, 297, 621
- Axon, D. J., Marconi, A., Capetti, A., Macchetto, F. D., Schreier, Robinson, A. 1998, *ApJ*, 496, L75
- Baldwin, J. A., Phillips, M. M., & Terlevich, R. 1981, *PASP*, 93, 5
- Bicknell, G. V., Dopita, M. A., Tsvetanov, Z. I., Sutherland, R. S. 1998, *ApJ*, 495, 680
- Binette, L., Wilson, A. S., & Storchi-Bergmann, T. 1996, *A&A*, 312, 365
- Boisson, C., Durret, F. 1986, *A&A*, 168, 32
- Cai, W. & Pradhan, A. K. 1993, *ApJS*, 88, 329
- Cardelli, J. A., Clayton, G. C., & Mathis, J. S., 1989, *ApJ*, 345, 245
- Colbert, E. J. M., Baum, S. A., Gallimore, J. F., O’Dea, C. P., Lehnert, M. D., Tsvetanov, Z. I., Mulchaey, J. S., and Caganoff, S. 1996a, *ApJS*, 105, 75
- Colbert, E. J. M., Baum, S. A., Gallimore, J. F., O’Dea, C. P., Christensen, J. A. 1996b, *ApJ*, 467, 551
- Colbert, E. J. M., Baum, S. A., O’Dea, Veilleux, S. 1998, *ApJ*, 496, 786
- Colina, L., Fricke, K. J., Kollatschny, W., & Perryman, M. A. C. 1987, *A&A*, 178, 51
- Dopita, M. A. & Sutherland, R. S. 1995, *ApJ*, 455, 468
- Dopita, M. A. & Sutherland, R. S. 1996, *ApJS*, 102, 161
- Dopita, M. A. 1997, *Ap&SS*, 248, 93
- Durret, F. 1990, *A&A*, 229, 351
- Durret, F., & Bergeron, J. 1988, *A&A*, Suppl. Ser. 75, 273
- Ferland, G. J., & Netzer, H. 1983, *ApJ*, 264, 105
- Glass, I. S. 1997, *MNRAS*, 292, L50
- Hummel, E., van Gorkom, J. H., & Kotanyi, C. G. 1983, *ApJ*, 267, L5
- Hutchmeier, W. K. 1982, *A&A*, 110, 121
- Koski, A. T. 1978, *ApJ*, 223, 56

- Lawrence, A. & Elvis, M. 1982, *ApJ*, 256, 410
- Malkan, M. A. 1983, *ApJ*, 264, L1
- Márquez, I., Boisson, C., Durret, F., and Petitjean, P. 1998, *A&A*, 333, 459
- Mendoza, C. 1983, in “Planetary Nebulae, I.A.U. Symposium No. 103” ed. D. R. Flower, (Dordrecht: D. Reidel), 143
- Metz, S. K., Tadhunter, C. N., Robinson, A., Axon, D. J. 1996, in *Emission Lines in Active Galaxies: New Methods and Techniques*, ed. B. M. Peterson, F.-Z. Cheng, and A. S. Wilson, *Astron. Soc. Pac. Conf. Ser. Vol. 113*, 390
- Penston, et al. 1990, *A&A*, 236, 53
- Pickles, A. J. 1985, *ApJS*, 59, 33
- Pogge, R. W. 1996, in *Emission Lines in Active Galaxies: New Methods and Techniques*, ed. B. M. Peterson, F.-Z. Cheng, and A. S. Wilson, *Astron. Soc. Pac. Conf. Ser. Vol. 113*, 378
- Robinson, A., Binette, L., Fosbury, R. A. E., Tadhunter, C. N. 1987, *MNRAS*, 227, 97
- Sanders, D. B., & Mirabel, I. F. 1985, *ApJ*, 298, L31
- Stasinska, G. 1984, *A&A*, 135, 341
- Storchi-Bergmann, T., Wilson, A. S., Mulchaey, J. S., & Binette, L. 1996, *A&A*, 312, 357
- Sutherland, R. S., Bicknell, G. V., & Dopita, M. A. 1993, *ApJ*, 414, 510
- Tadhunter, C. N., Robinson, A., & Morganti, R. 1989, in *Extranuclear Activity in Galaxies*, ed. E. J. A. Meurs & R. A. E. Fosbury (Garching: ESO), 293
- Taylor, D., Dyson, J. E. & Axon, D. J. 1992, *MNRAS*, 255, 351
- Terlevich, R., Tenorio-Tagle, G., Franco, J., Melnick, J. 1992, *MNRAS*, 255, 713
- Tsvetanov, Z., Dopita, M., Allen, M. 1995, *BAAS*, 27, 871
- Ulvestad, J. S., Wilson, A. S. 1984, *ApJ*, 285, 439
- Unger, S. W., Pedlar, A., Axon, D. J., Whittle, M., Meurs, E. J. A., & Ward, M. 1987, *MNRAS*, 228, 671
- Ward, M., Penston, M. V., Blades, J. C., & Turtle, A. J. 1980, *MNRAS*, 193, 563
- Ward, M. J., Geballe, T., Smith, M., Wade, R., Williams, P. 1987, *ApJ*, 316, 138
- Weaver, K et al. 1996, *ApJ*, 458, 160

Wehrle, A. E., Morris, M. 1988, *AJ*, 95, 1689

Wilson, A. S., Ward, M. J. & Haniff, C. A. 1988, *ApJ*, 334, 121

Veilleux, S., Osterbrock, D. E. 1987, *ApJS*, 63, 295.

Viegas, S. M., de Gouveia Dal pino, E. M. 1992, *ApJ*, 384, 467

Table 1. Line intensities of NGC 2992

Line	NW cone		SE cone		inter-cone	
	Flux	Flux (r.c)	Flux	Flux (r.c)	Flux	Flux (r.c)
(1)	(2)	(3)	(4)	(5)	(6)	(7)
[Ne V] $\lambda$ 3426	560 $\pm$ 12	81 $\pm$ 17	61 $\pm$ 20	130 $\pm$ 40	...	...
[O II] $\lambda$ 3727	440 $\pm$ 20	610 $\pm$ 30	423 $\pm$ 15	802 $\pm$ 28	62 $\pm$ 3	176 $\pm$ 9
[Ne III] $\lambda$ 3869	95 $\pm$ 35	125 $\pm$ 46	100 $\pm$ 8	180 $\pm$ 10	50 $\pm$ 20	130 $\pm$ 70
H <sub>8</sub> + He I $\lambda$ 3888	22 $\pm$ 9	29 $\pm$ 12	...	...	...	...
[Ne III] $\lambda$ 3967	31 $\pm$ 11	40 $\pm$ 15	...	...	...	...
[S II] $\lambda$ 4072	...	...	9 $\pm$ 5	14 $\pm$ 8	...	...
H $\delta$	22 $\pm$ 8	27 $\pm$ 9	16 $\pm$ 5	26 $\pm$ 8	24 $\pm$ 11	49 $\pm$ 24
H $\gamma$	42 $\pm$ 4	49 $\pm$ 4	37 $\pm$ 6	51 $\pm$ 8	55 $\pm$ 13	84 $\pm$ 21
[O III] $\lambda$ 4363	15 $\pm$ 3	17 $\pm$ 3	16 $\pm$ 6	21 $\pm$ 7	...	...
He II $\lambda$ 4686	28 $\pm$ 4	29 $\pm$ 4	32 $\pm$ 7	35 $\pm$ 7	...	...
H $\beta$	100 $\pm$ 6	100 $\pm$ 6	100 $\pm$ 6	100 $\pm$ 6	100 $\pm$ 10	100 $\pm$ 10
[O III] $\lambda$ 4959	320 $\pm$ 20	310 $\pm$ 20	290 $\pm$ 40	280 $\pm$ 40	70 $\pm$ 5	65 $\pm$ 5
[O III] $\lambda$ 5007	950 $\pm$ 60	920 $\pm$ 60	910 $\pm$ 120	840 $\pm$ 100	220 $\pm$ 18	194 $\pm$ 16
[N I] $\lambda$ 5200	7 $\pm$ 2	7 $\pm$ 2	...	...	...	...
He I $\lambda$ 5876	31 $\pm$ 12	26 $\pm$ 10	63 $\pm$ 15	42 $\pm$ 10	52 $\pm$ 17	27 $\pm$ 9
[O I] $\lambda$ 6300	40 $\pm$ 3	32 $\pm$ 3	90 $\pm$ 14	54 $\pm$ 8	56 $\pm$ 11	24 $\pm$ 5
[O I] $\lambda$ 6363	19 $\pm$ 3	14 $\pm$ 2	37 $\pm$ 17	20 $\pm$ 10	...	...
[N II] $\lambda$ 6548	63 $\pm$ 1	48 $\pm$ 1	143 $\pm$ 4	79 $\pm$ 2	163 $\pm$ 2	63 $\pm$ 1
H $\alpha$	410 $\pm$ 5	310 $\pm$ 3	560 $\pm$ 10	310 $\pm$ 8	810 $\pm$ 10	310 $\pm$ 4
[N II] $\lambda$ 6583	189 $\pm$ 4	142 $\pm$ 3	430 $\pm$ 10	237 $\pm$ 7	490 $\pm$ 7	185 $\pm$ 3
[S II] $\lambda$ 6716	123 $\pm$ 6	91 $\pm$ 5	230 $\pm$ 20	120 $\pm$ 10	220 $\pm$ 32	79 $\pm$ 11
[S II] $\lambda$ 6731	95 $\pm$ 5	71 $\pm$ 4	180 $\pm$ 20	98 $\pm$ 9	174 $\pm$ 25	62 $\pm$ 9
[S III] $\lambda$ 9069	67 $\pm$ 5	38 $\pm$ 3	83 $\pm$ 42	25 $\pm$ 13	251 $\pm$ 27	37 $\pm$ 4
[S III] $\lambda$ 9532	197 $\pm$ 11	109 $\pm$ 6	300 $\pm$ 70	90 $\pm$ 20	512 $\pm$ 44	68 $\pm$ 6

Note. — All intensities are given relative to H $\beta$ =100. (r.c) indicates reddening corrected intensities.

Table 2.

Region	$L_{40}([\text{O III}])$	$L_{40}(\text{H}\alpha)$	$\log_{10} Q_{rec}$
NW cone	5.01	1.9	53.2
SE cone	5.63	3.7	53.5
NW cone (red corrected)	14.4	4.2	53.5
SE cone (red corrected)	76.9	29.9	54.4
Entire EELR	11.7	6.70	53.0
Entire EELR (red corrected)	96.0	40.1	53.8

Note. — Luminosities of the NW, SE and inter-cone regions of NGC 2992 in units of  $10^{40}$  ergs  $\text{s}^{-1}$ , and the inferred rate of hydrogen recombinations  $Q_{rec}$  ( $\text{s}^{-1}$ ).



Fig. 1.— Optical and radio images of NGC 2992: a) [O III]  $\lambda 5007$  narrow band image, b)  $H\alpha + [N II]$  narrow band image, c) blue continuum image, d) blue continuum image overlaid with the 20cm radio map from Hummel et al. (1983) (contours: -2, 2, 4, 7, 10, 20, 30, 50, 70, 90, 110 mJy per beam; beam=6'') e) [O III] narrow band image overlaid with 20cm radio contours, f) [O III] overlaid with the 6cm radio map from Ulvestad and Wilson (1984) (contours: 3, 6, 9, 15, 30, 50, 70, 90% of the peak of 7.2 mJy per beam; beam=0.5'').

Fig. 2.— Slit positions used for the long-slit observations of NGC 2992 overlaid on the [O III]  $\lambda 5007$  contour map with contour levels shown at 0.5, 1, 2, 5, 10, 20, 40, 60, 80, 100% of the peak value.

Fig. 3.— a) Average spectrum of the NW cone of NGC 2992, b) Average spectrum of the SE cone of NGC 2992, c) Spectrum of the inter-cone region of NGC 2992.

Fig. 4.— Blue spectra of the NW and SE cones of NGC 2992. The top curve shows the observed spectrum overlaid with the template used to subtract the underlying stellar contribution. The lower curve shows the template subtracted spectrum.

Fig. 5.— Spatial variation of line ratios in NGC 2992. The open circles indicate line ratios from positions in the NW cone, solid squares indicate points in the SE cone, and open triangles indicate the inter-cone region as shown in Figure 6.

Fig. 6.— Spatial locations of the extracted spectra overplotted on the [O III]  $\lambda 5007$  contour map. The contour levels are as in Figure 2. The open circles indicate positions in the NW cone, solid squares indicate points in the SE cone, and open triangles indicate the inter-cone region.

Fig. 7.—  $H\alpha + [N II] \lambda 6548, 6583$  profiles in the spectra of the NW cone (top), SE cone (center), and the inter-cone regions (lower). In each panel we show the total fit overlaid on the data template subtracted data. The lighter weight curves show the fitted galaxy template and the individual Gaussian component fits to the  $H\alpha$  and [N II] emission lines.

Fig. 8.— Electron densities  $n_e$  inferred from the [S II]  $\lambda 6717/\lambda 6731$  ratio in spectra extracted from various positions in the ENLR of NGC 2992. The plotting symbols represent the different regions of the ENLR as shown in Figure 6.

Fig. 9.— Ionization parameter estimated from the [O III]/[O II] line ratio at each point in the spectral map of NGC 2992. The plotting symbols represent the different regions of the ENLR as shown in Figure 6.

Fig. 10.— [O III]  $\lambda 5007/H\alpha$  versus [N II]  $\lambda 6583/H\alpha$ . The observed line ratios are shown for each point in the spectral map of the ENLR of NGC 2992. The plotting symbols represent the different regions of the ENLR as shown in Figure 6; open circles denote points from the NW cone, solid squares denote points from the SE cone, and open triangles indicate the inter-cone region. In panel (a) we over-plot the shock, and shock+precursor model grids and also include the average  $1\sigma$  error bar and a vector which indicates the direction of reddening correction. The shock and

shock+precursor model grids are labelled with shock velocity in units of  $\text{km s}^{-1}$ , and with the magnetic parameter  $B/n^{1/2} = 0-4$  in units of  $\mu\text{G cm}^{3/2}$ . Panel (b) shows the single component photoionization ( $\alpha=-1.0,-1.4$  and  $-2.0$ )  $U$ -sequences plotted for  $n = 100 \text{ cm}^{-3}$  and  $n = 1000 \text{ cm}^{-3}$  with grid lines of constant  $U$  every 0.25 dex, and labelled with  $\log_{10}U$ . The  $A_{M/I}$  sequence is also shown and is labelled with  $A_{M/I}$  and has tick marks at 0.2 dex intervals.

Fig. 11.— [O III]  $\lambda 5007/\text{H}\alpha$  versus [N II]  $\lambda 6583/\text{H}\alpha$ . The data points and model grids are as described for Figure 10.

Fig. 12.— [O III]  $\lambda 5007/\text{H}\beta$  versus [S II]  $\lambda\lambda 6717,6731/\text{H}\alpha$ . The data points and model grids are as described for Figure 10.

Fig. 13.— [O III]  $\lambda 5007/\text{H}\beta$  versus [O II]  $\lambda 3727/[\text{O III}] \lambda 5007$ . The data points and model grids are as described for Figure 10.

Fig. 14.— [N II]  $\lambda 6583/\text{H}\alpha$  versus [S II]  $\lambda\lambda 6717,6731/\text{H}\alpha$ . The data points and model grids are as described for Figure 10.

Fig. 15.— [O I]  $\lambda 6300/[\text{O III}] \lambda 5007$  versus [O II]  $\lambda 3727/[\text{O III}] \lambda 5007$ . The data points and model grids are as described for Figure 10.

Fig. 16.— [S III]  $\lambda\lambda 9069,9532/\text{H}\alpha$  versus [S II]  $\lambda\lambda 6717,6731/\text{H}\alpha$ . In panel (a) the shock-only grid is shown with the dashed line. The data points and model grids are otherwise as described for Figure 10.

Fig. 17.— [S II]  $\lambda\lambda 6717,6731/\text{H}\alpha$  versus He II  $\lambda 4686/\text{H}\beta$ . In panel (a) the shock-only grid is shown with the dashed line. The line ratios for the average spectra of the NW and SE cones are shown as the open circle, and the solid square respectively. The model grids are as described for Figure 10.

Fig. 18.— He II  $\lambda 4686/\text{H}\beta$  versus [O II]  $\lambda 3727/[\text{O III}] \lambda 5007$ . The line ratios for the average spectra of the NW and SE cones are shown as the open circle, and the solid square respectively. The shock, shock+precursor,  $U$ -sequence and  $A_{M/I}$  sequence models are shown and are labelled as described in Figure 10.

Fig. 19.— [Ne V]  $\lambda 3426/[\text{Ne III}] \lambda 3869$  versus [O III]  $\lambda 5007/\text{H}\beta$  ratio. The line ratios for the average spectra of the NW and SE cones are shown with the open circle, and the solid square respectively. The shock, shock+precursor,  $U$ -sequence and  $A_{M/I}$  sequence models are shown and are as described in Figure 10.

Fig. 20.— Temperature sensitive diagnostic diagram: [O III]  $\lambda 4363/[\text{O III}] \lambda 5007$  versus He II  $\lambda 4686/\text{H}\beta$ . The  $R_{OIII}$  temperature scale is shown on the left side of the diagram. The line ratios for the average spectra of the NW and SE cones are shown with the open circle, and the solid square respectively. The shock, shock+precursor,  $U$ -sequence and  $A_{M/I}$  sequence models are shown and are as described in Figure 10.

Fig. 21.— Densities (a), and Ionization parameters (b) for points within the NW and SE cone regions that were used in the  $q$ -test calculations.

Fig. 22.—  $Q$  versus radius, and  $n_{e,Q}$  versus radius for three different de-projections of the points within the ionization cones of NGC 2992. The diagrams in the left panels show  $Q$  versus radius for de-projection onto the near side for both cones (top), de-projection onto the far side of the cones (middle) and with no de-projection (bottom). The diagrams in the right panels show the corresponding plots of  $n_{e,Q}$  versus radius. The plotting symbols represent the different regions of the ENLR as shown in Figure 6. The lower useful limit for the [S II] density diagnostic is shown with the dashed line in the diagrams in the right panels.

Fig. 23.— a) Outflow velocity field overplotted on the [O III]  $\lambda 5007$  contour map. The size of the circle at each point indicates the difference in velocity of the wind component relative to the rotational component. The key in the top right hand corner indicates the magnitude of this velocity in  $\text{km s}^{-1}$ . Solid points correspond to velocities that are blue shifted relative to the rotation, and open circles indicate red shifted velocities. b) FWHM map of the major outflow component. The image contours are the same as in Figure 2.

Fig. 24.— Excitation versus line width diagrams. (a): [O III]  $\lambda 5007/\text{H}\beta$  versus the FWHM of the kinematical components. The kinematical component identified with the galaxy rotation is plotted as the solid circles, the main outflow components are plotted as open squares and the extra component (detected at a few locations) is plotted as open triangles. (b): [N II]  $\lambda 6583/\text{H}\alpha$  versus FWHM. As in (a), the square points indicate the main outflow component, and the triangles indicate the extra component. In (b) we make the distinction between the cones by using filled symbols for the SE cone and open symbols for the NW cone. In both (a) and (b) the solid curve is the shock+precursor model prediction where the FWHM is directly related to the shock velocity, and the dashed curve assumes that the FWHM is associated with the projection of randomly oriented shocks so that  $V_{shock} \simeq \text{FWHM}/\sqrt{3}$ . The uncertainty in the FWHM is generally less than  $100 \text{ km s}^{-1}$ .

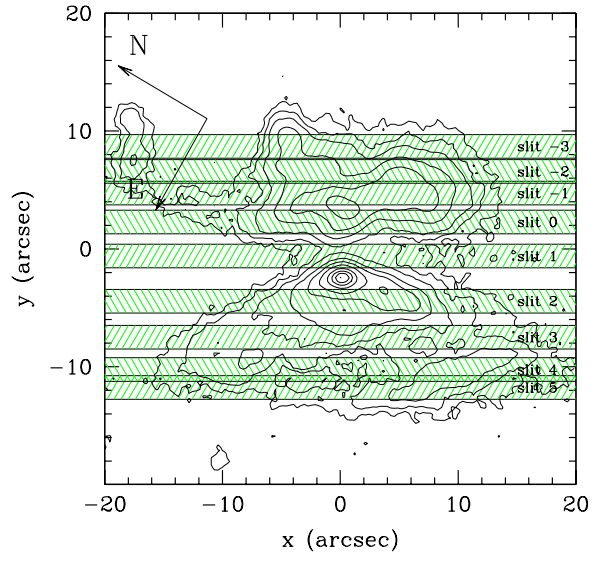


Figure 2

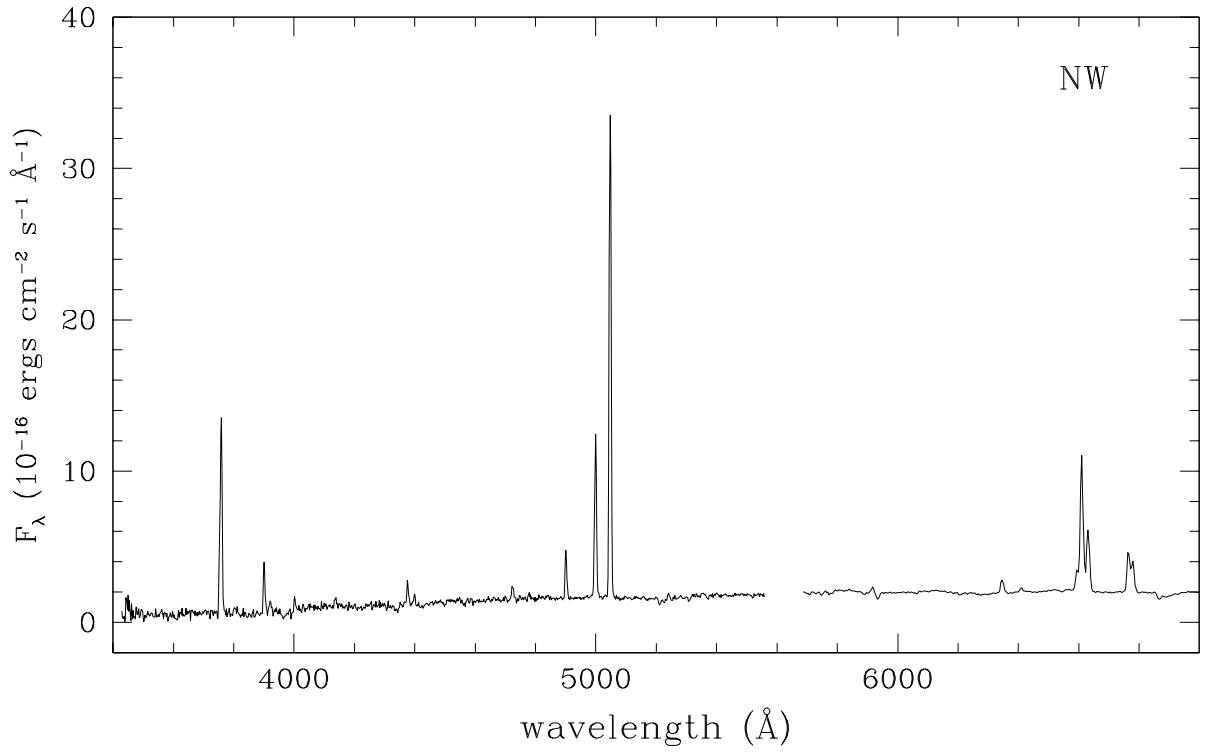


Figure 3a

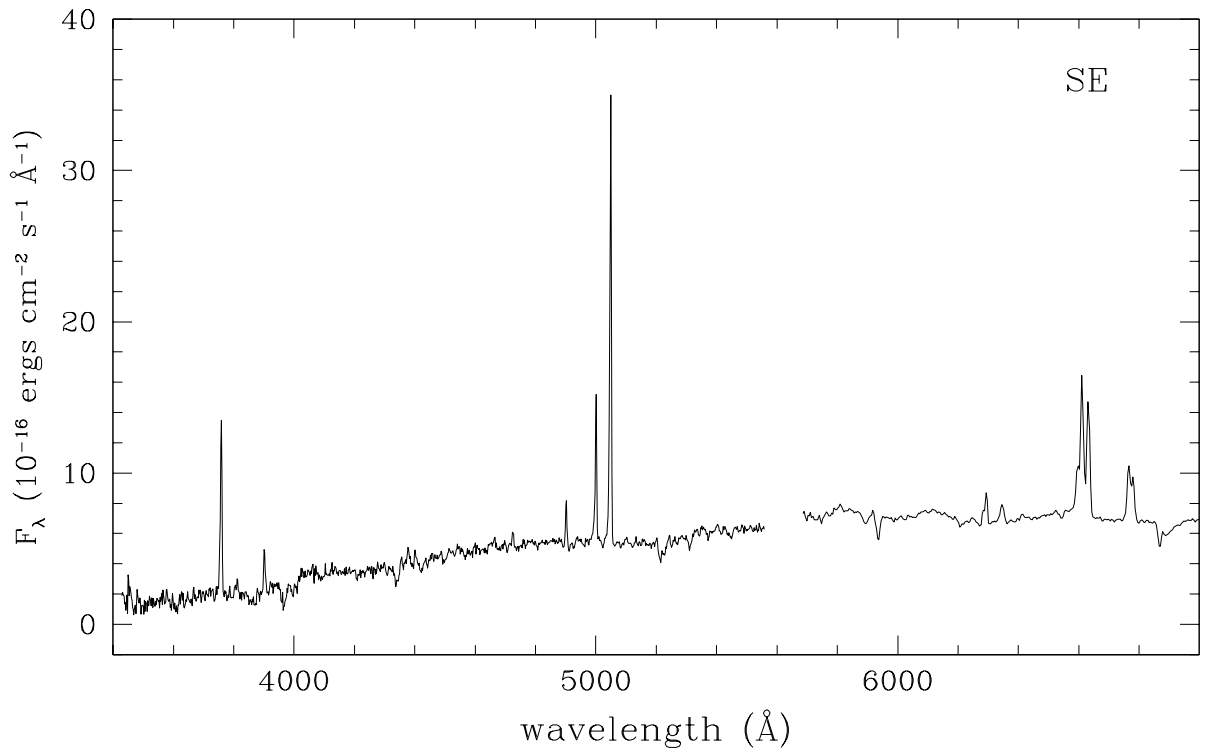


Figure 3b

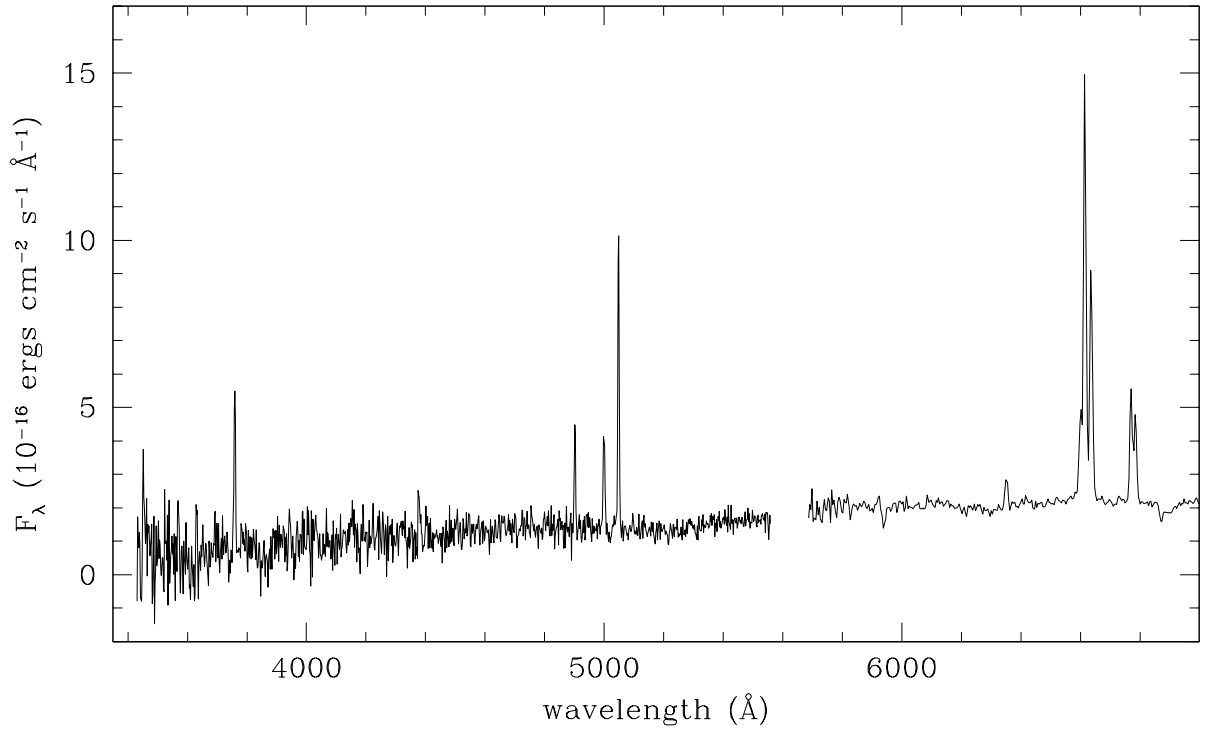


Figure 3c

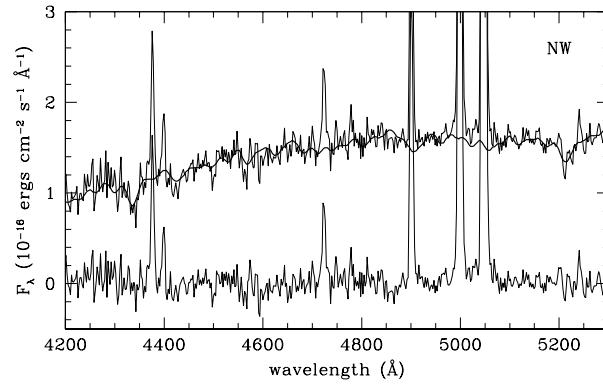


Figure 4a

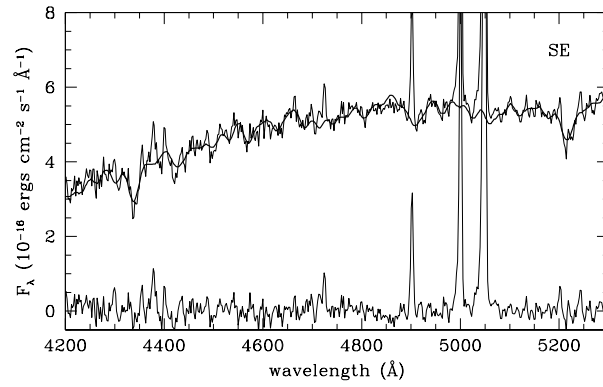


Figure 4b



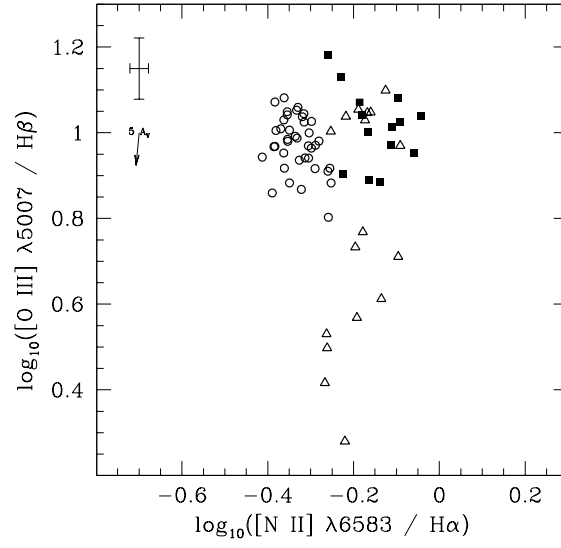


Figure 5a

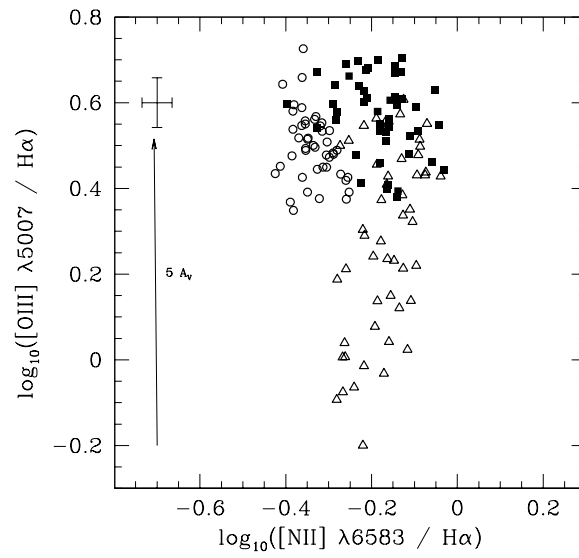


Figure 5b

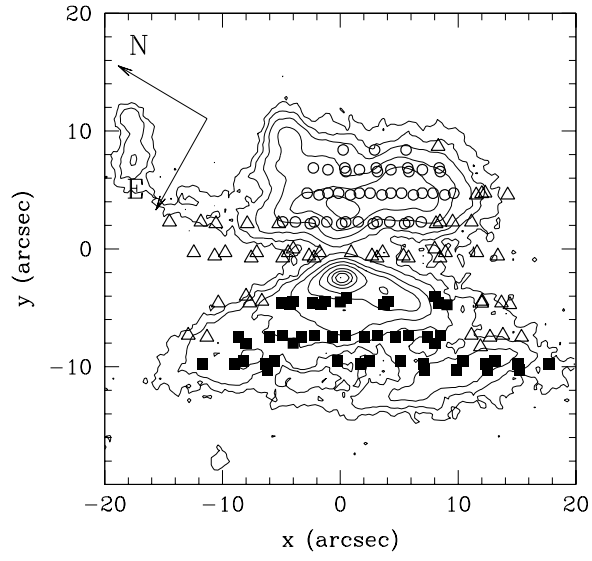


Figure 6

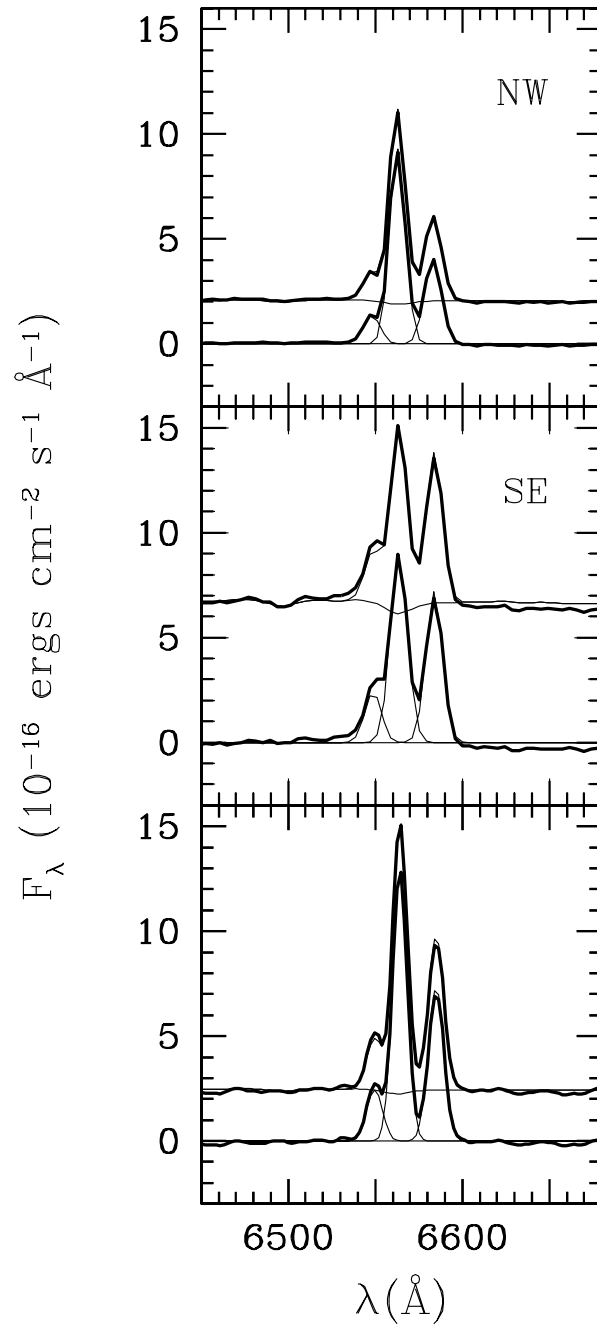


Figure 7

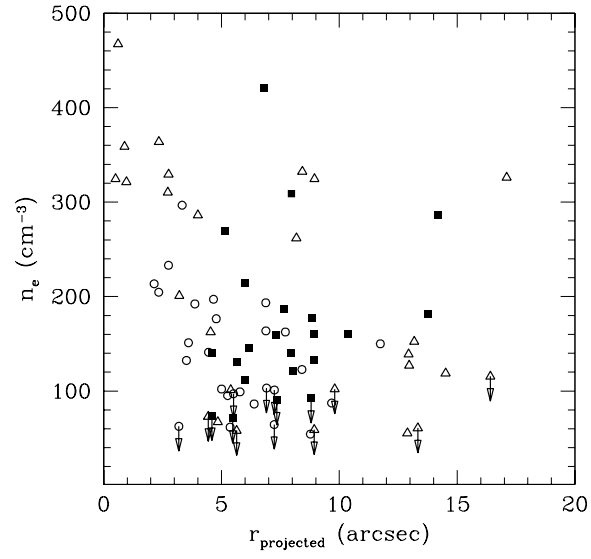


Figure 8

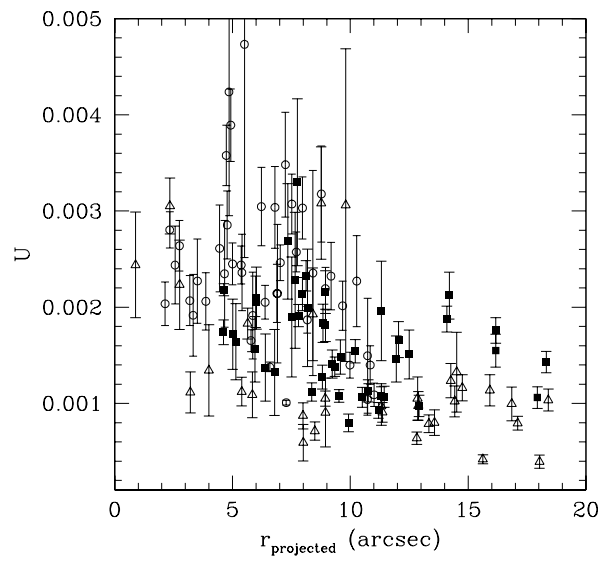


Figure 9

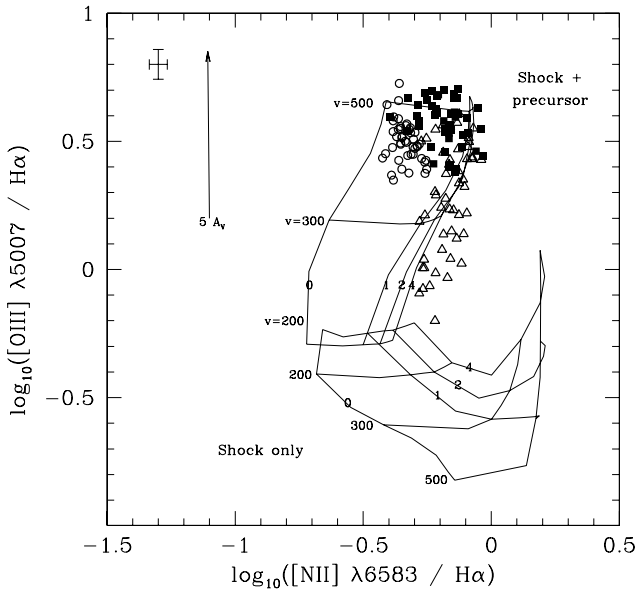


Figure 10a

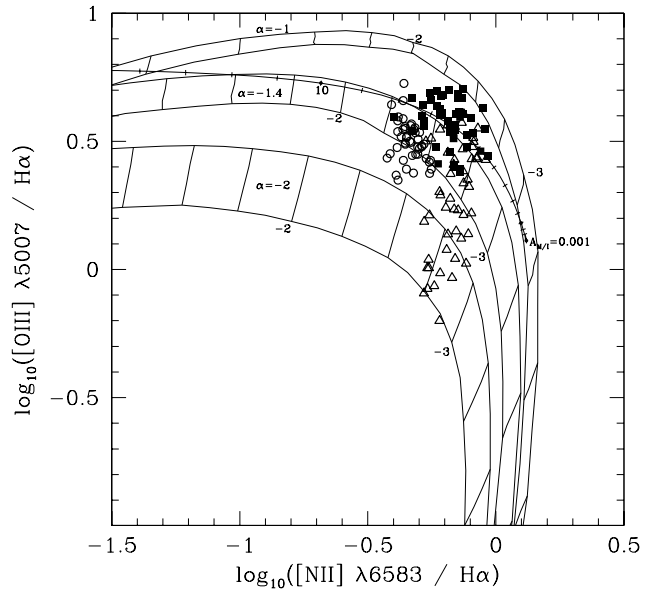


Figure 10b

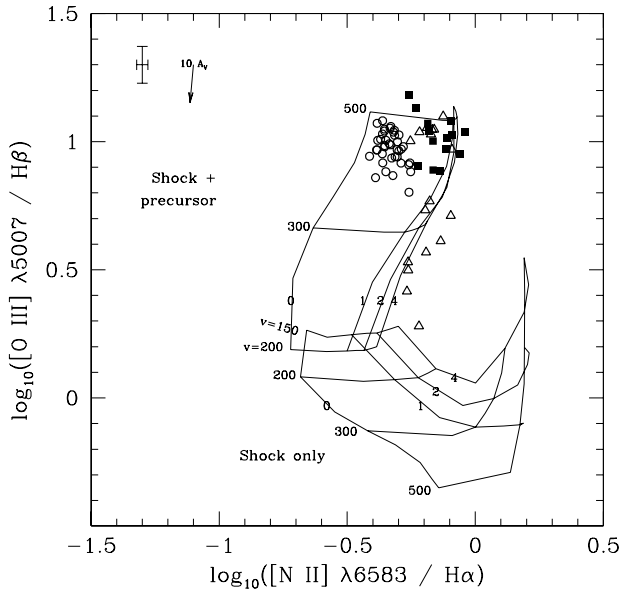


Figure 11a

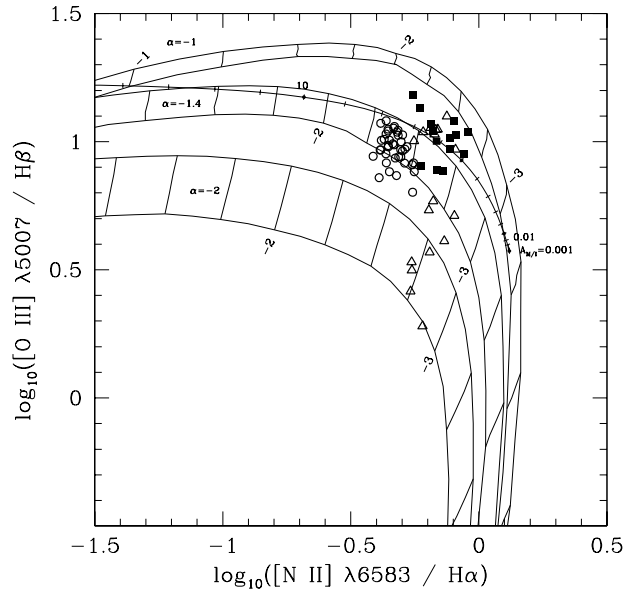


Figure 11b

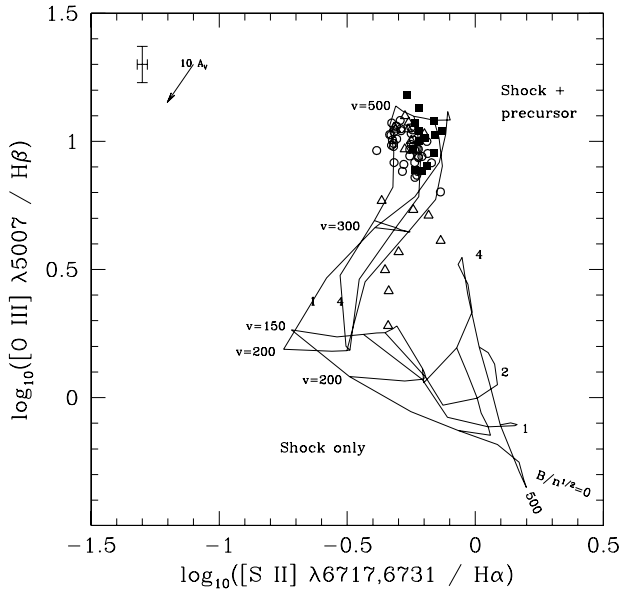


Figure 12a

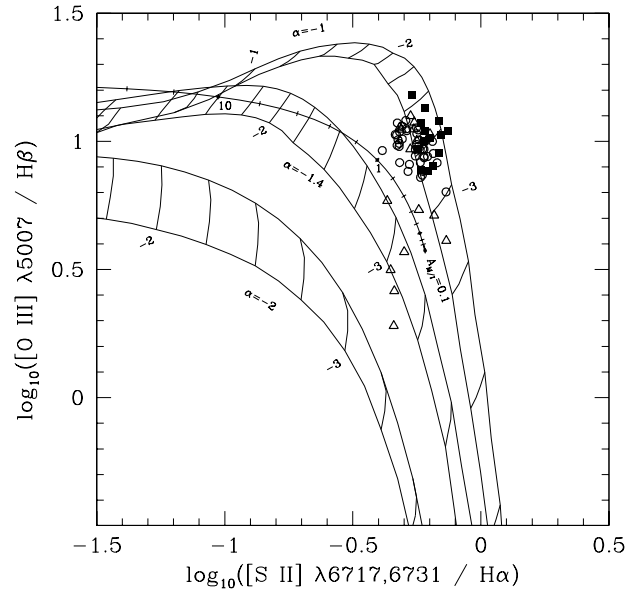


Figure 12b

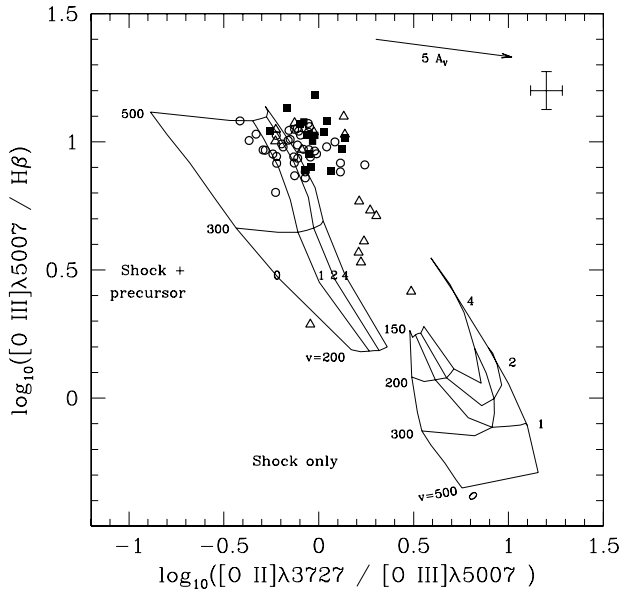


Figure 13a

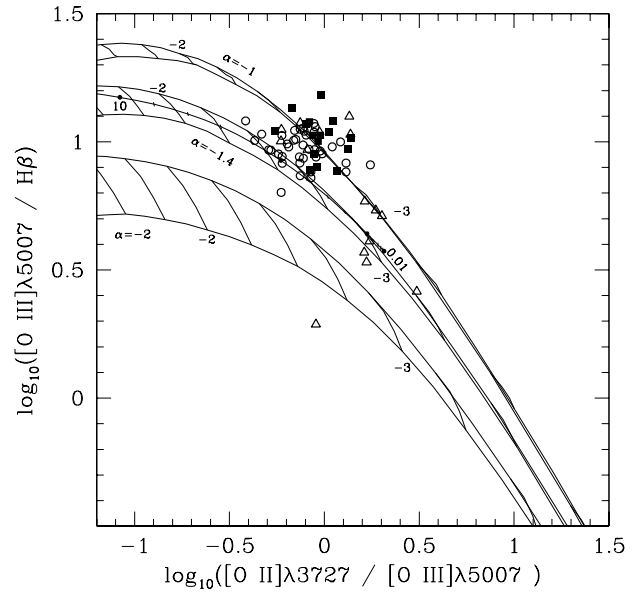


Figure 13b

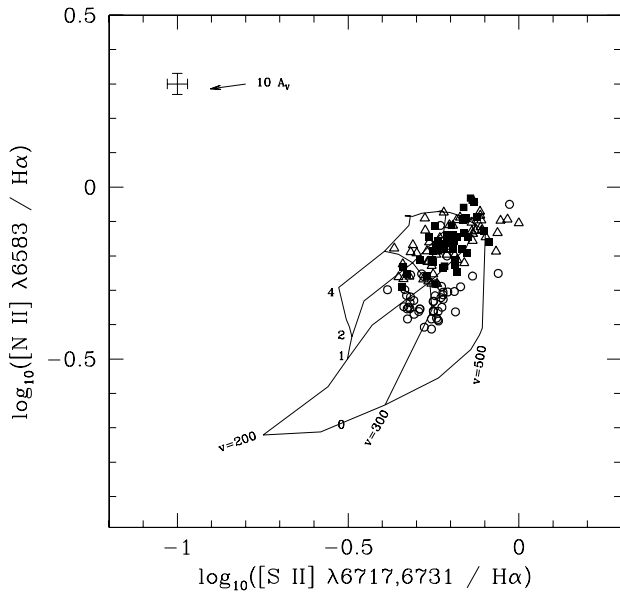


Figure 14a

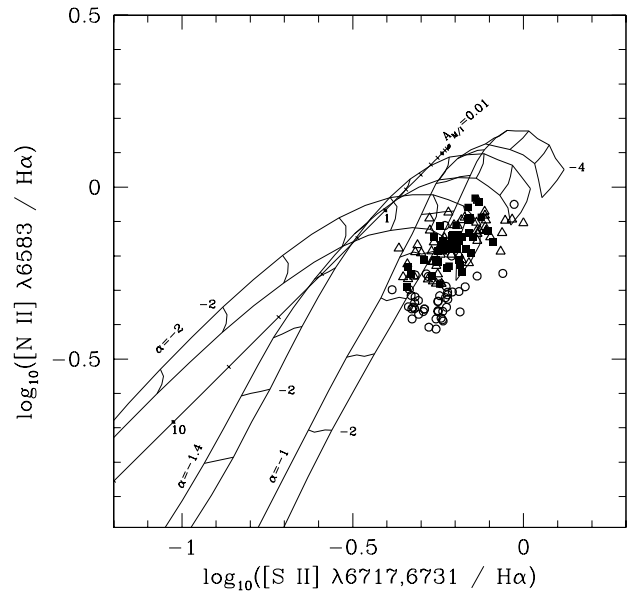


Figure 14b

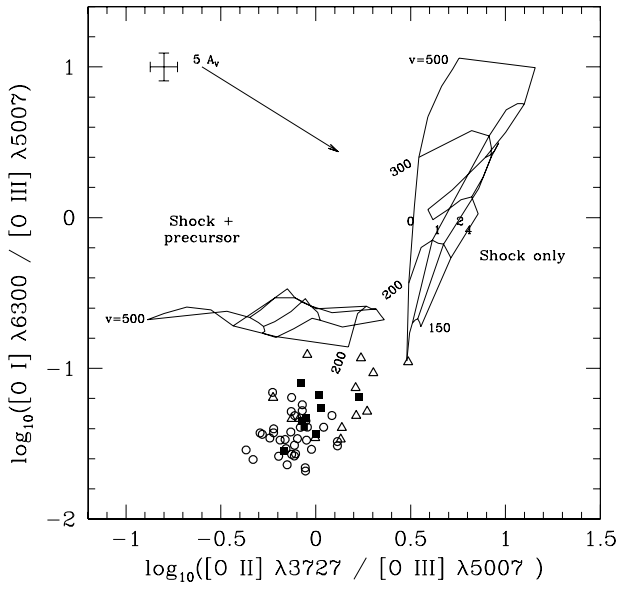


Figure 15a

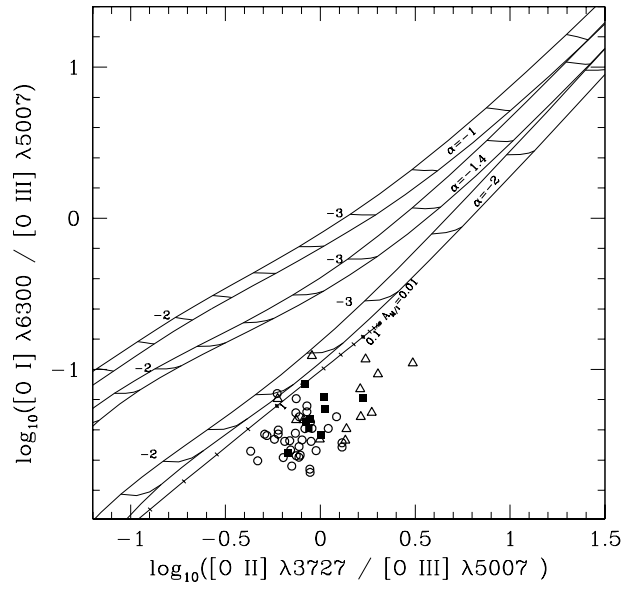


Figure 15b

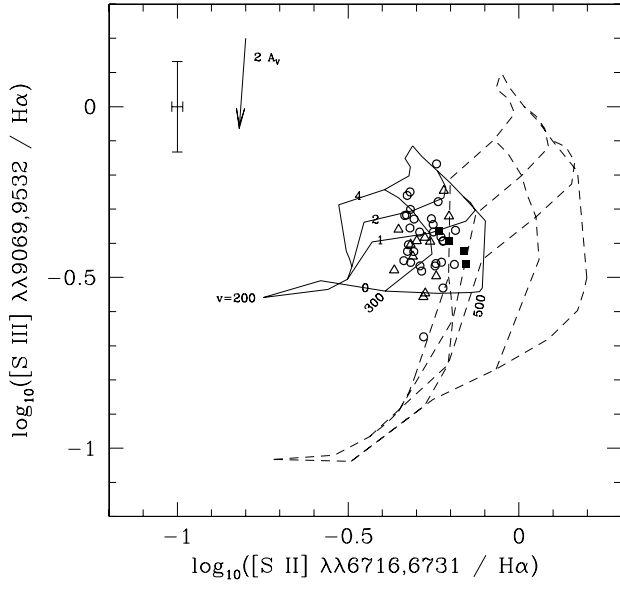


Figure 16a

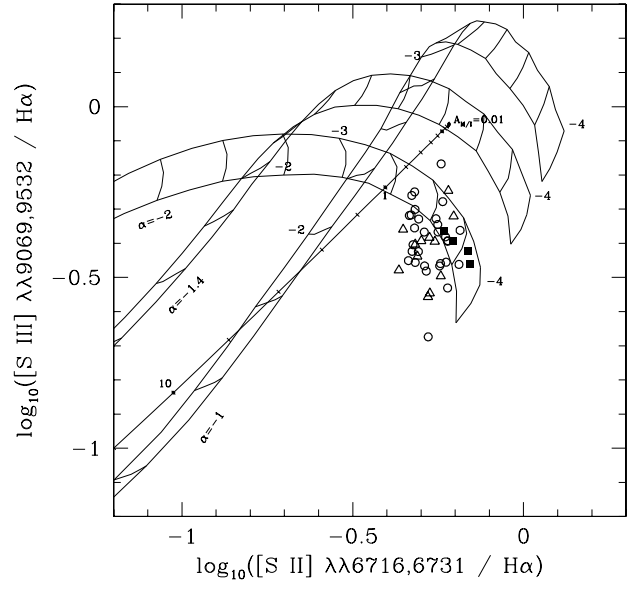


Figure 16b

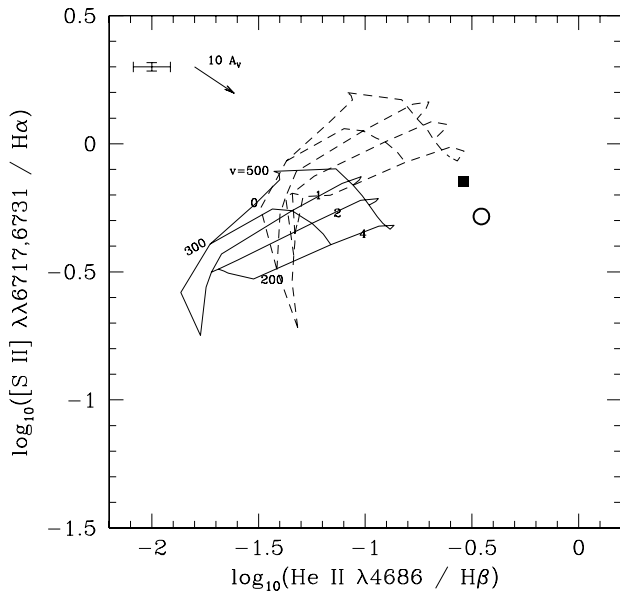


Figure 17a

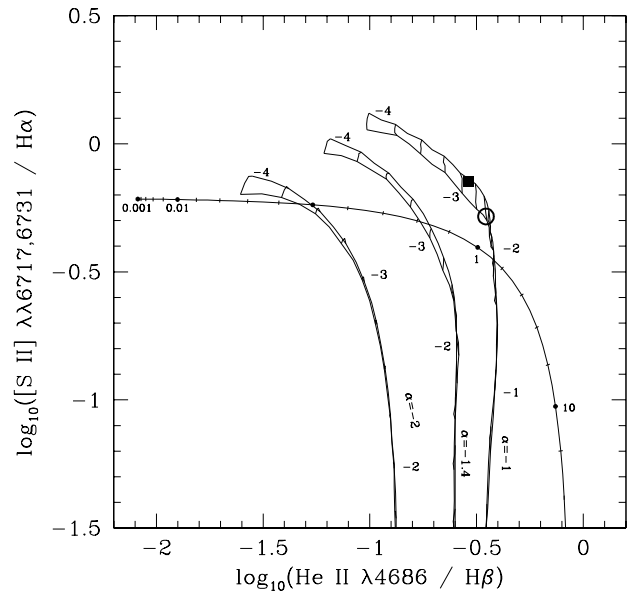


Figure 17b



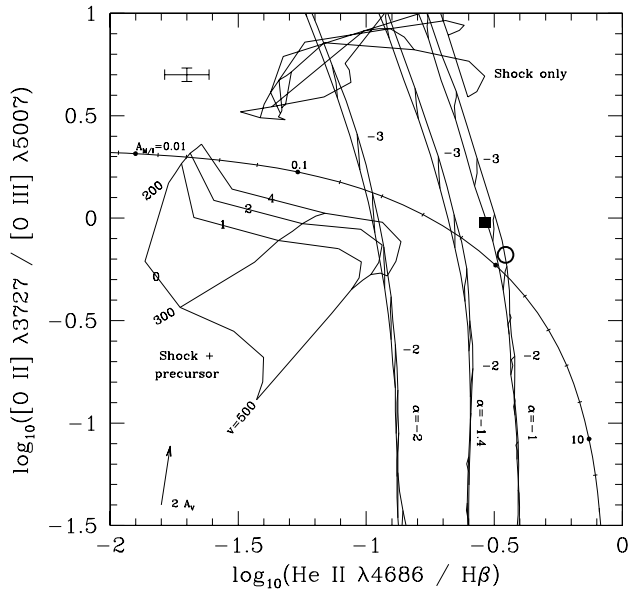


Figure 18

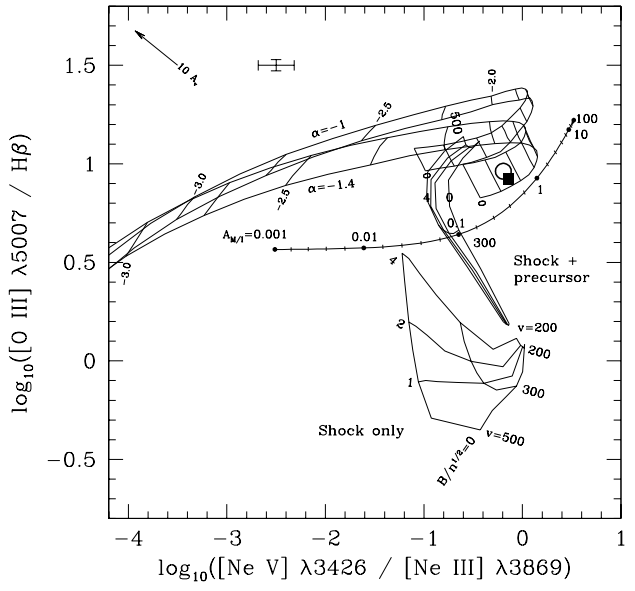


Figure 19

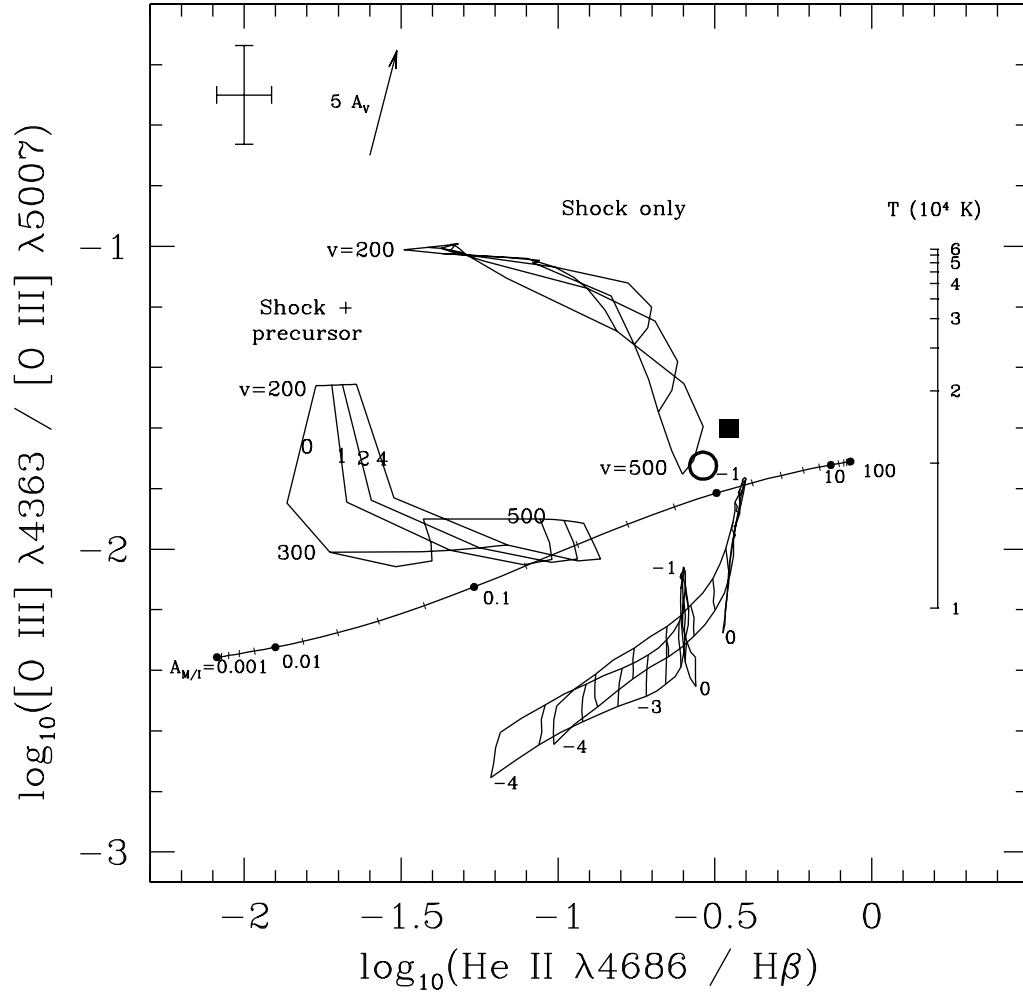


Figure 20

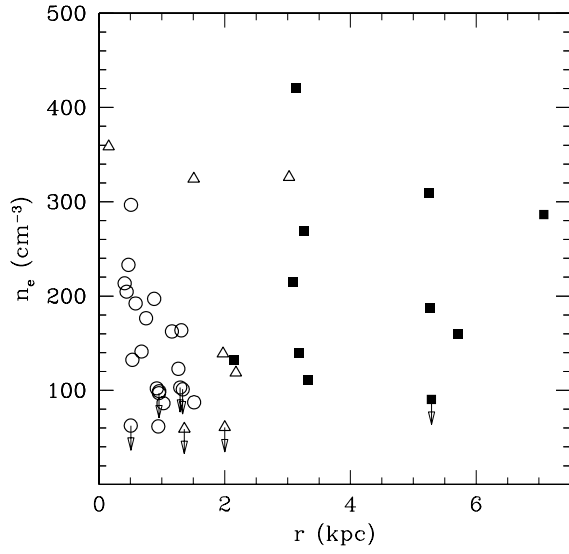


Figure 21a

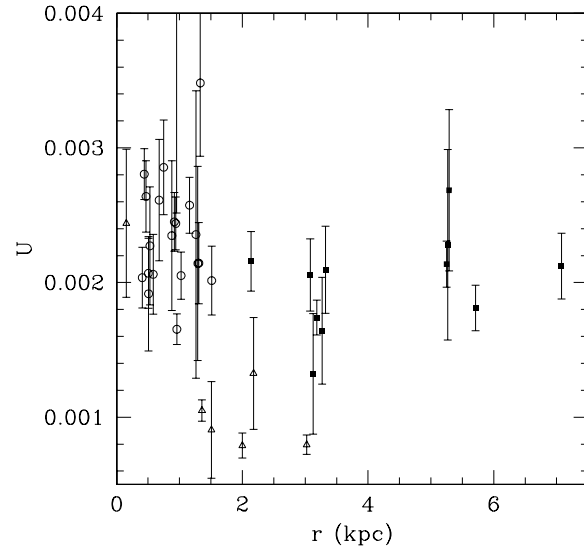


Figure 21b

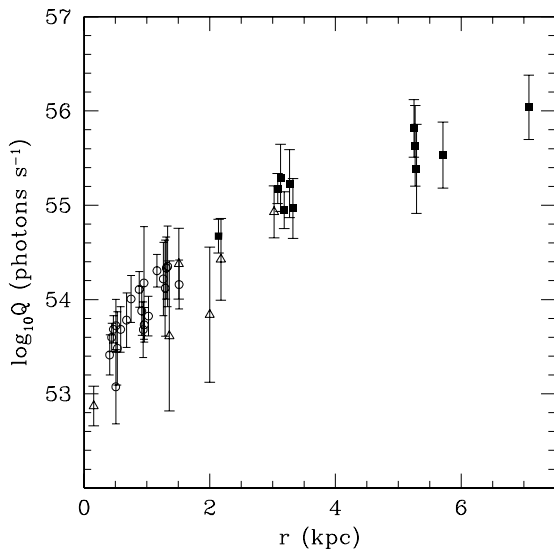


Figure 22a

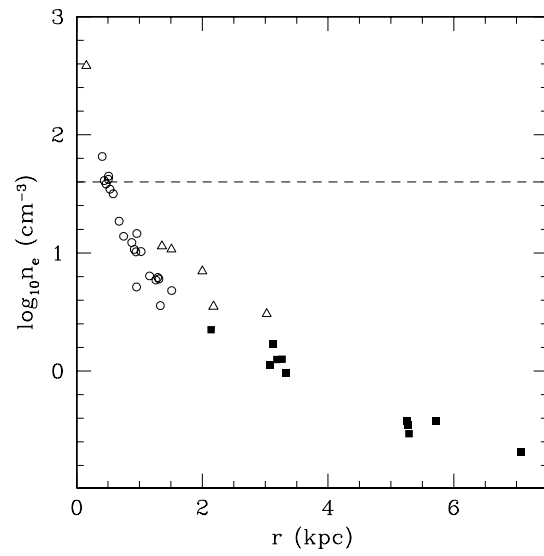


Figure 22b

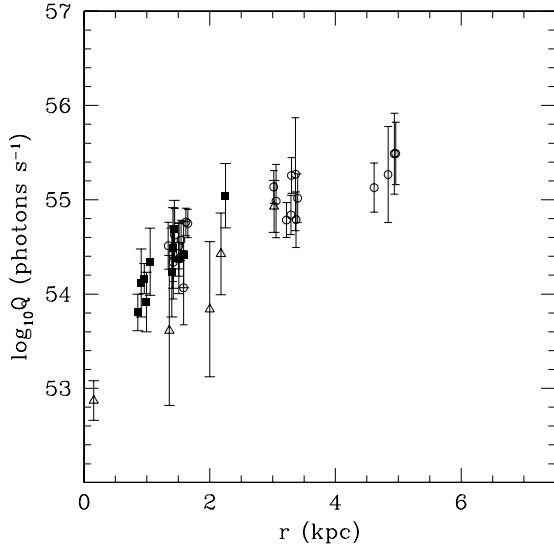


Figure 22c

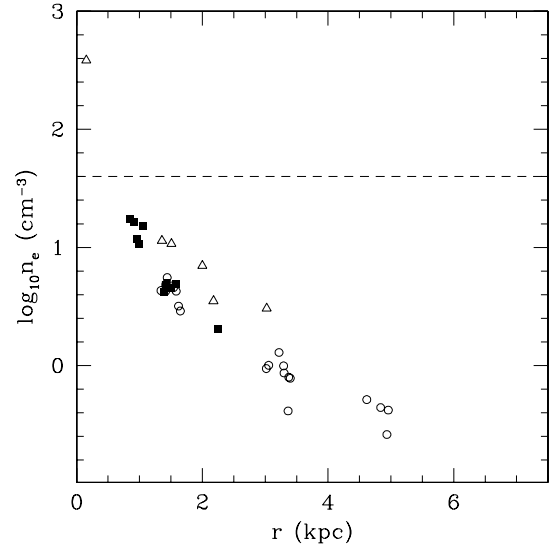


Figure 22d

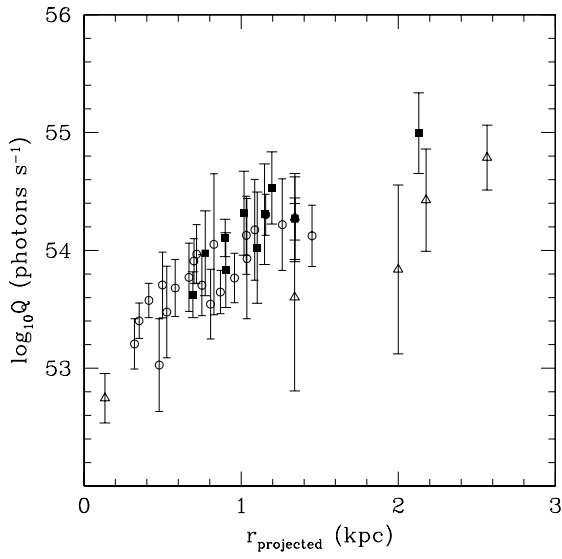


Figure 22e

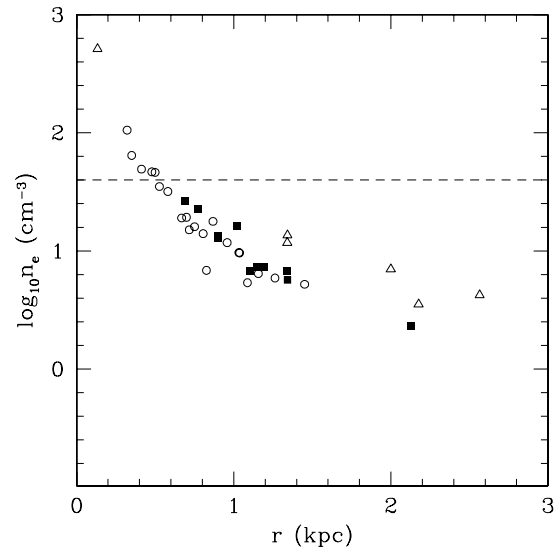


Figure 22f

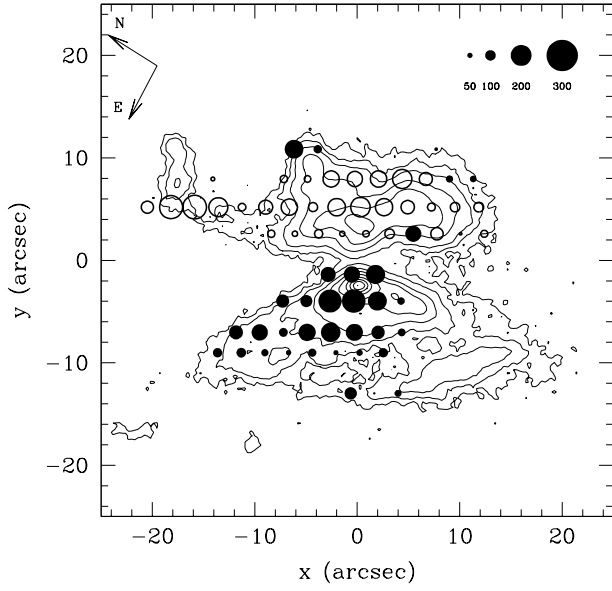


Figure 23a

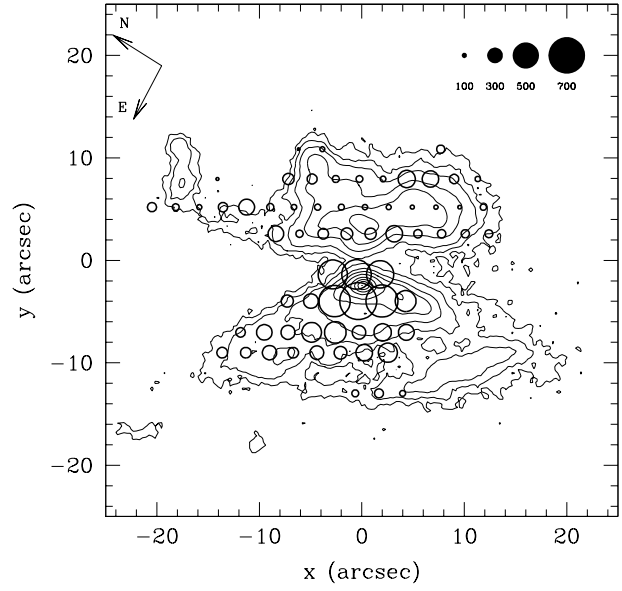


Figure 23b

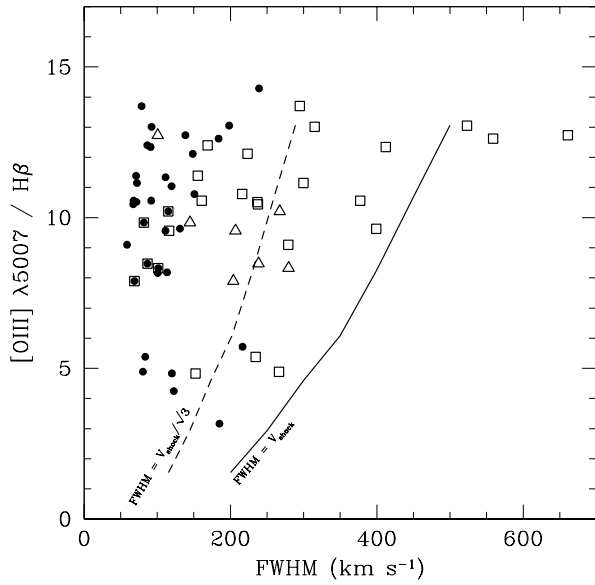


Figure 24a

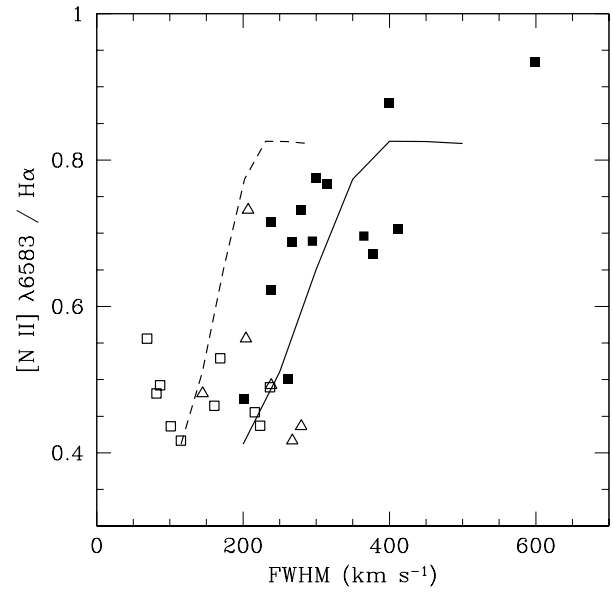


Figure 24b

This figure "fig1a.jpg" is available in "jpg" format from:

<http://arxiv.org/ps/astro-ph/9809123v1>

This figure "fig1b.jpg" is available in "jpg" format from:

<http://arxiv.org/ps/astro-ph/9809123v1>

This figure "fig1c.jpg" is available in "jpg" format from:

<http://arxiv.org/ps/astro-ph/9809123v1>



This figure "fig1d.jpg" is available in "jpg" format from:

<http://arxiv.org/ps/astro-ph/9809123v1>

This figure "fig1e.jpg" is available in "jpg" format from:

<http://arxiv.org/ps/astro-ph/9809123v1>

This figure "fig1f.jpg" is available in "jpg" format from:

<http://arxiv.org/ps/astro-ph/9809123v1>